

Search for gravitational waves from five low mass X-ray binaries in the second Advanced LIGO observing run with an improved hidden Markov model

Hannah Middleton,^{1,2,*} Patrick Clearwater,^{1,2,3} Andrew Melatos,^{1,2} and Liam Dunn^{1,2}

¹*School of Physics, University of Melbourne, Parkville, Vic, 3010, Australia*

²*OzGrav-Melbourne, Australian Research Council Centre of Excellence for Gravitational Wave Discovery, Parkville, Victoria, 3010, Australia*

³*Data61, Commonwealth Scientific and Industrial Research Organisation, Corner Vimiera & Pembroke Roads, Marsfield NSW 2122, Australia*

(Dated: June 26, 2020)

Low mass X-ray binaries are prime targets for continuous gravitational wave searches by ground-based interferometers. Results are presented from a search for five low-mass X-ray binaries whose spin frequencies and orbital elements are measured accurately from X-ray pulsations: HETE J1900.1-2455, IGR J00291+5934, SAX J1808.4-3658, XTE J0929-314, and XTE J1814-338. Data are analysed from Observing Run 2 of the Advanced Laser Interferometer Gravitational-wave Observatory (LIGO). The search algorithm uses a hidden Markov model to track spin wandering, the \mathcal{J} -statistic maximum likelihood matched filter to track orbital phase, and a suite of five vetoes to reject artefacts from non-Gaussian noise. The search yields a number of low-significance, above threshold candidates consistent with the selected false-alarm probability. The candidates will be followed up in subsequent observing runs.

DOI:

I. INTRODUCTION

Ground-based gravitational-wave observatories such as Advanced LIGO [1] and Advanced Virgo [2] are searching for persistent, periodic gravitational wave (GW) signals. One of the key targets for these continuous-wave (CW) searches are rotating neutron stars. At the present time, GWs have been observed from transient events comprising binary black hole [3–7] and binary neutron star [8, 9] coalescences, but no CW signal has been detected. However the GW spectrum has only just been opened. Future CW detections will shed light on a number of fundamental physics questions, including the properties of bulk nuclear matter [10, 11].

Low mass X-ray binaries (LMXBs) are of particular interest for CW searches. LMXBs are composed of a compact object (such as a neutron star or stellar mass black hole) with a low mass stellar companion (typically $\lesssim 1M_{\odot}$) [12–14]. Within these binaries, matter is transferred from the low mass star to the neutron star, spinning it up. Electromagnetic (EM) observations show that these accreting neutron stars rotate below the centrifugal break-up frequency. Torque balance between spin up via accretion and spin down via GW emission is one way to explain the frequency distribution observed [15].

Scorpius X-1 is a prime LMXB target for CW searches by Advanced LIGO and Advanced Virgo. Scorpius X-1 shines brightly in X-rays, indicating a high accretion rate and potentially strong CW emission. Extensive searches have been made for Scorpius X-1 with multiple search pipelines and data sets from Initial LIGO and

Initial Virgo [16–20]¹. Scorpius X-1 was also targeted in the first Advanced LIGO Observing Run (O1) from September 2015 to January 2016 [21–23], and the second Advanced LIGO Observing Run (O2) [24, 25]. O2 started in November 2016 with the LIGO instruments and was joined by Virgo for the final month before the run ended in August 2017. To date, no CW detection has been made. However upper limits have been placed on the GW strain from Scorpius X-1, the best being the cross-correlation search which gives a 95% confidence upper limit on the strain of $h_0^{95\%} \lesssim 2.3 \times 10^{-25}$ at 175 Hz [23, 26].

Searches for CWs from Scorpius X-1 and other LMXBs face a number of challenges. First, the rotation frequency of the compact object wanders significantly during the observation. A hidden Markov model (HMM) has the ability to track the wandering efficiently and accurately. Following Refs. [24, 27, 28], this is the approach we apply in this paper. A second challenge is that the rotation frequency is sometimes unknown from EM observations. For Scorpius X-1, no EM pulsations have been observed from the system [29]. Wide band searches need to be carried out, e.g. the recent O2 Scorpius X-1 search spanned 60–650 Hz [24].

Many LMXBs do have EM observations of pulsations, whose frequencies are measured with an accuracy of $\sim 10^{-8}$ Hz. It is these targets we focus on for this search. EM observations of pulsations greatly reduce the computational cost of the search, making these targets appealing for CW searches despite their lower X-ray brightness in comparison to Scorpius X-1.

* hannah.middleton@unimelb.edu.au

¹A search for LMXB XTE J1751-305 was also made with Initial LIGO [20].

In this work we search data from O2, focusing only on data from the two LIGO observatories (due to the shorter duration of the Virgo data in O2). We present a search for five LMXB targets with well known rotation frequencies. The search method is identical to that used in Ref. [24]. We briefly review it in Sec. II. The target list is described in Sec. III and the searched parameter ranges in Sec. IV. We describe the application of this search to LMXB targets in Sec. V and Sec. VI. The results are presented in Sec. VII, followed by a brief discussion of the expected strain from LMXBs in Sec. VIII. The conclusions are summarized in Sec. IX.

II. SEARCH ALGORITHM

The LMXB search follows the same procedure as the O2 search for Scorpius X-1 [24]. Here we briefly review the search method, which is described in full in Refs. [21, 24, 27, 28].

A. HMM

In a Markov process, the probability of occupying the current state depends only on the previous state. In a hidden Markov process, the state is unobservable. The LMXB targets of this search have observed spin frequencies. However, we note that a drift may exist between the rotation of the crust (where EM pulsations originate) and the core (which may or may not dominate the GW-emitting mass or current quadrupole) [28, 30]. The CW frequency is therefore hidden.

Following the notation in Ref. [24], we label the hidden state variable as $q(t)$. This state transitions between some set of allowed values $\{q_1, \dots, q_{N_Q}\}$ at times $\{t_0, \dots, t_{N_T}\}$. The probability of jumping from q_i at time t_n to q_j at t_{n+1} is given by a transition matrix $A_{q_j q_i}$ which depends only on $q(t_n)$. Measurements are made of some observable with allowed values $\{o_i, \dots, o_{N_o}\}$, and an emission matrix $L_{o_j q_i}$ relates the likelihood that an observation of o_j relates to a hidden state q_i . In a CW search, the observable is the interferometer data or some data product generated from it, e.g. a Fourier transform, or detection statistic.

The total duration of the observation is T_{obs} . When searching for LMXBs, the observation is divided into N_T equal parts, each of length $T_{\text{drift}} = T_{\text{obs}}/N_T$. Identically to Ref. [24], we take $T_{\text{drift}} = 10$ days (other HMM searches use a shorter T_{drift} depending on the type of target [31–33]). For each segment, $L_{o_j q_i}$ is calculated from some frequency domain estimator, such as the \mathcal{F} -statistic or \mathcal{J} -statistic as discussed in Sec. II B.

Given an estimator, the probability that an observation $O = \{o(t_0), \dots, o(N_T)\}$ is associated with a partic-

ular hidden path $Q = \{q(t_0), \dots, q(N_T)\}$ is

$$P(Q|O) = L_{o(t_{N_T})q(t_{N_T})} A_{q(t_{N_T})q(t_{N_T-1})} \cdots L_{o(t_1)q(t_1)} \times A_{q(t_1)q(t_0)} \Pi_{q(t_0)}, \quad (1)$$

where $\Pi_{q(t_0)}$, the prior (i.e. the probability that the system starts in q_i at $t = t_0$), is taken to be uniform. Our objective is to find the optimal hidden path Q^* maximizing $P(Q|O)$. The Viterbi algorithm [34] achieves this in a computationally-efficient way by avoiding an exhaustive search of all paths. It is applied in Refs. [21, 24, 27, 28] to CW searches.

The Viterbi detection score [21] for a given path is defined as the number of standard deviations the path's log likelihood exceeds the mean log likelihood of all paths in a user-selected frequency sub-band containing the path's end state. The quantity $\delta_{q_i}(t_{N_T})$ is defined as the likelihood of the most likely path ending in state q_i at step N_T . The mean and standard deviation of $\ln \delta_{q_i}(t_{N_T})$, marginalized over a sub-band, are given by

$$\mu_{\ln \delta}(t_{N_T}) = \frac{1}{N_Q} \sum_{i=1}^{N_Q} \ln \delta_{q_i}(t_{N_T}), \quad (2)$$

$$\sigma_{\ln \delta}^2(t_{N_T}) = \frac{1}{N_Q} \sum_{i=1}^{N_Q} [\ln \delta_{q_i}(t_{N_T}) - \mu_{\ln \delta}(t_{N_T})]^2. \quad (3)$$

The Viterbi score for the path with the highest likelihood at step N_T , i.e. δ_{q^*} for $q^* = \arg \max_i \delta_{q_i}(t_{N_T})$, is then

$$S = \frac{\ln \delta_{q^*} - \mu_{\ln \delta}(t_{N_T})}{\sigma_{\ln \delta}(t_{N_T})}. \quad (4)$$

As in Refs. [21, 24], we use the Viterbi score as our detection statistic throughout this paper.

B. \mathcal{J} -statistic

A frequency domain estimator is used to convert the detector data into the probability that a signal is present at a frequency f . CW searches are carried out over many months, so the estimator must account for the motion of the Earth around the Solar System barycenter. The \mathcal{F} -statistic [35] is an example of an estimator used as a matched filter in CW searches for isolated neutron stars.

In a binary the signal is Doppler modulated by the binary motion. The orbital component of the phase varies with time t as

$$\Phi_s(t) = -2\pi f_* a_0 \sin \Omega (t - t_a), \quad (5)$$

where f_* is the rotation frequency of the star, a_0 is the projected semi-major axis, $\Omega = 2\pi/P$ is the orbital angular velocity with orbital period P , and t_a is some reference time usually chosen to be the time of passage of the ascending node T_{asc} . The \mathcal{J} -statistic introduced in Ref. [27] extends the \mathcal{F} -statistic matched filter to include

binary orbital modulation. The orbital motion spreads the \mathcal{F} -statistic power into orbital sidebands spaced by $1/P$ and centred on f_* . The \mathcal{J} -statistic weights and sums these sidebands given a set of three binary parameters: P , a_0 and T_{asc} . The sum is performed coherently with respect to orbital phase. We make the assumption of circular orbits. As in Ref. [24], we use the \mathcal{J} -statistic as our estimator for this search.

III. TARGETS

The targets of this search are LMXBs. In LMXBs, f_* is measured from X-ray observations of pulsations or burst oscillations [36]. Accreting millisecond pulsars (AMSPs) are a subclass of LMXBs that can exhibit intermittent X-ray pulsations. These sources make interesting targets for CW searches because, in many cases, f_* is measured to better than 10^{-8} Hz. (Again, we emphasise that the signal frequency is not necessarily equal to f_* ; see Sec. II A). Generally, AMSPs are transient; they have ‘active’ (outburst) and ‘quiescent’ phases. We denote the spin frequency of the star in its active and quiescent phases as f_{act} and f_{qu} respectively and use f_* as a general label for the spin frequency in either phase, whenever there is no need to distinguish between f_{act} and f_{qu} . As discussed in Sec. VIII, the frequency derivative \dot{f}_* has implications for the anticipated signal strength.

The traditional picture is that the active phase is associated with accretion onto the neutron star. Pulsations are often observed during outburst, whereupon f_{act} and the \dot{f}_{act} can be measured directly. Active phases can last from weeks to years. Some sources pulsate persistently throughout the active phase, whilst others pulsate intermittently [37]. In the active phase, \dot{f}_{act} is set by the accretion torque [38].

During quiescence, pulsations are not observed. However, \dot{f}_{qu} can be inferred from the difference in f_{act} measured during the neighbouring active epochs. In quiescence, \dot{f}_{qu} is usually set by magnetic dipole braking, although there may still be accretion taking place during these periods [39].

CW emission is possible during both active and quiescent phases. Torque balance is possible when the gravitational radiation reaction torque cancels the accretion torque. It is also possible for the star to spin up or down under the action of positive or negative hydromagnetic accretion torques [38, 40]. Radiation reaction may contribute to a negative \dot{f}_{act} or \dot{f}_{qu} . Equally, if a positive \dot{f}_{act} or \dot{f}_{qu} is observed, say due to accretion, it may outweigh and therefore mask a negative torque due to gravitational radiation reaction.

Deformations in the neutron star which are not aligned with the rotation axis produce CW emission. Neutron star mountains can be formed by magnetic stresses misaligned with the spin axis [41–44] and thermo-elastic deformations of a relativistic star [45]. Another emission mechanism involves r-modes (Rossby waves due to the

Coriolis effect). The r-mode oscillations are predicted to be excited by radiation-reaction instabilities and can persist into quiescence [46, 47].

An overview of the known accreting neutron stars, as well as their prospects as GW targets, can be found in Ref. [36]. Below we briefly introduce the five sources we analyse in this paper. The LMXB targets in this search have distances between 3.4–8.0 kpc; see also sections III A–III E. All targets are further away than Scorpius X-1 (2.8 ± 0.3 kpc [29]). However, they are less than three times further away, so the wave strain should be comparable to Scorpius X-1, if the quadrupole moment and f_* are comparable too. The binary properties are collated in Table I.

A. HETE J1900.1-2455

HETE J1900.1-2455 was first observed in outburst in 2005 by HETE-II (High Energy Transient Explorer-2) [55]. It has distance estimates of ~ 4.3 kpc [56] and 4.7 ± 0.6 kpc [57]. Early observations by RXTE (Rossi X-ray Timing Explorer) revealed X-ray pulsations which were detected continuously for 22 d but became intermittent and then undetectable [49, 58]. A spin-orbit model [59] was used to compute a fit for the orbital parameters and pulsation frequency, yielding 377.296171971(5) Hz for the latter quantity. On MJD 53559 (8 July 2005) a brightening in the source flux was observed as well as a shift in frequency to 377.291596(16) Hz, after which pulsations became suppressed [49]. The source remained in outburst without observed pulsations for ~ 10 years until its return to quiescence in 2015 [60]. In this paper we use the timing solution in Ref. [49] computed from the period before the spin jump, when pulsations were observed. There is no frequency derivative measured.

B. IGR J00291+5934

IGR J00291+5934 is the fastest known AMSP at 598.89213053(2) Hz. Distance estimates yield a lower limit of 4 kpc and an upper limit of 6 kpc from Refs. [61] and [62] respectively. It was discovered in a 14 d outburst in 2004 [51, 63]. Searches in the RXTE All Sky Monitor data indicate marginal evidence for two prior outbursts during 1998 and 2001 [64, 65]. A double outburst was observed in 2008, lasting 9 d in August and 15 d in September [66, 67]. The most recent outburst in 2015 lasted 25 d. A timing solution for the spin and orbital parameters was computed from the 2015 outburst in Ref. [50, 65]. Several estimates of \dot{f}_* exist from active and quiescent periods (see Table IV). In this paper we use the timing solution from Ref. [50].

TABLE I: Target list: position (right ascension and declination), orbital period (P), projected semi-major axis (a_0 in light-seconds), time of ascension (T_{asc}), and frequency of observed pulsations (f_*). Quoted errors (in parentheses) are the 1σ uncertainties apart from XTE J1814-338, where they indicate the 90% confidence interval from Ref. [48].

Target	RA	Dec	P (s)	a_0 (lt-s)	T_{asc} (GPS time)	f_* (Hz)	Refs.
HETE J1900.1-2455	19h00m08.65s	$-24^\circ 55' 13.7''$	4995.258(5)	0.01841(1)	803 963 261.3(6)	377.296171971(5)	[49]
IGR J00291+5934	00h29m03.05s	$+59^\circ 34' 18.93''$	8844.08(2)	0.0649905(24)	1 122 114 624.0(3)	598.89213053(2)	[50, 51]
SAX J1808.4-3658	18h08m27.62s	$-36^\circ 58' 43.3''$	7249.143(4)	0.062810(3)	1 112 750 818.84(23)	400.9752090(1)	[52, 53]
XTE J0929-314	09h29m20.19s	$-31^\circ 23' 03.2''$	2614.746(3)	0.006290(9)	705 152 406.1(9)	185.105254297(9)	[54]
XTE J1814-338	18h13m39.03s	$-33^\circ 46' 22.3''$	15388.7229(2)	0.390633(9)	739 049 211.59(8)	314.35610879(1)	[48]

C. SAX J1808.4-3658

SAX J1808.4-3658 is a regular outburst discovered in 1996 by the *BeppoSAX* satellite [68] with an estimated distance in the range 3.4–3.6 kpc [69]. Eight outbursts have been observed, the most recent of which was in 2019 [70]. As the 2019 outburst occurred after O2, we use the most recent outburst prior to O2 which began in April 2015 [53]. In Ref. [53] the spin and orbit parameters are computed from observations of the 2015 outburst by XMM-Newton and NuSTAR (Nuclear Spectroscopic Telescope Array). XMM-Newton and NuSTAR yield frequencies of 400.9752090(1) Hz and 400.975214(1) Hz respectively. Several observations of \dot{f}_* have been made in both active and quiescent phases (see Table IV). In this paper, we use the timing solution from Ref. [53].

D. XTE J0929-314

XTE J0929-314 was discovered in outburst during two months in April–June 2002 by RXTE [54], the only outburst observed to date [71]. It has an estimated distance > 7.4 kpc [71]. The spin and orbital parameters were computed from RXTE timing data. There is also an estimate of \dot{f}_* during the active phase [54]. The pulsation frequency is 185.105254297(9) Hz with $\dot{f}_{\text{act}} = -9.2(4) \times 10^{-14}$ Hz s $^{-1}$ (spin down). In this paper we use the timing solution in Ref. [54].

E. XTE J1814-338

XTE J1814-338 was discovered in outburst in 2003 [72] by RXTE. The outburst lasted 53 d and is the only one observed. Distance estimates range from 3.8 kpc [73] to ~ 8 kpc [74]. The spin and orbital parameters were computed via timing analysis. Pulsations at 314.35610879(1) Hz were observed with $\dot{f}_{\text{act}} = -6.7(7) \times 10^{-14}$ Hz s $^{-1}$. In this paper we use the timing solution from Ref. [48].

IV. SPIN, ORBITAL, AND ASTROMETRIC PARAMETERS

A targeted CW search requires the sky position [right ascension (RA) and declination (Dec)] of the source, needed for the \mathcal{J} -statistic to account for the motion of the Earth with respect to the target. To apply the \mathcal{J} -statistic, three binary orbital parameters are also necessary: the orbital period P , the projected semi-major axis a_0 , and the orbital phase ϕ_a . The phase of the orbit from X-ray observations is often quoted as the time of the ascending node T_{asc} where the Doppler-shifted frequency of the neutron star is lowest (the phase is also sometimes quoted as the time of inferior conjunction of the companion star, $T_{90} = T_{\text{asc}} + P/4$ [36, 54]). In this search we use T_{asc} for all targets. EM observations of pulsations constrain the neutron star spin frequency f_* .

The electromagnetically determined search parameters are summarized in Table I. Observations of X-ray pulsations during active phases are able to directly constrain f_* to high precision. The uncertainties in f_* are typically small, as Table I shows. However, signal frequency is not necessarily identical to f_* (see also Sec. II A and Sec. V B). Timing solutions inferred from the Doppler-shifted pulsations allow the orbital parameters to be constrained (see P , a_0 , and T_{asc} in Table I).

There are several mechanisms which can lead to CW emission from a rotating neutron star as described in Sec. III. Thermal or magnetic ‘mountains’ emit at $2f_*$ and possibly f_* [15]. R-mode oscillations emit at $\sim 4f_*/3$ [46, 47, 75]. Pinned superfluids emit at f_* [76] and $2f_*$ [77]. We also search for signals at $f_*/2$, where harmonics may exist. In summary, we search bands containing $\{1/2, 1, 4/3, 2\} f_*$ for each target as discussed in Sec. V B.

Identically to Ref. [24], we choose a sub-band size of ~ 0.61 Hz (see Sec. V for details). Previous CW searches have used sub-bands in the range 0.01–1 Hz depending on the target, algorithm, and search type (e.g. all sky, targeted) [23, 78–81].

Recent developmental work on r-mode searches recommends scanning a relatively wide frequency range around

the $4f_*/3$ value [82]. For the targets considered here, we calculate the recommended search band using Eq. (17) in Ref. [82]. XTE J1814-338 has the narrowest band (253–291 Hz), and IGR J00291+5934 has the widest band (669–940 Hz). The ~ 0.61 Hz sub-bands searched in this paper are deliberately chosen to be narrower than these ranges. An exhaustive, broadband, r-mode search across hectohertz frequencies lies outside the scope of this paper, whose central objective is to conduct fast, narrowband searches at a selection of sensible harmonics of f_* , taking advantage of well-measured EM observables in LMXBs for the first time. We postpone a broadband r-mode search to future work (see also Ref. [83] for a recent r-mode search).

The search ranges for the orbital parameters are based on the uncertainty in the EM measurement. In many cases, the orbital parameters are known to high accuracy, reducing the computational cost. The error in T_{asc} is typically < 1 s. However, the uncertainty in both T_{asc} and P means that the extrapolation becomes more unreliable the further it extends. If T_{asc} is measured several years before O2, we can use P to calculate a time when the binary returns to the same position in its orbit close to the O2 start time (at $T_{\text{O2,start}} = 1164562334$). To propagate the combined error, we compute the number of orbits N_{orb} between the observed T_{asc} and the time of ascension just before the start of O2 from

$$T_{\text{asc,O2}} = T_{\text{asc}} + N_{\text{orb}}P, \quad (6)$$

and the error for the propagated T_{asc} is

$$\sigma_{T_{\text{asc,O2}}} = [\sigma_{T_{\text{asc}}}^2 + (N_{\text{orb}}\sigma_P)^2]^{1/2}, \quad (7)$$

where σ_P and $\sigma_{T_{\text{asc}}}$ are the errors on P and T_{asc} respectively. For all targets we choose to use 3σ uncertainties, except for XTE J0929-314 where we search a T_{asc} range equal to its orbital period ($T_{\text{asc}} \pm P/2$). This search range achieves good coverage of the parameter space whilst keeping the computational cost manageable. The $T_{\text{asc,O2}}$ values used in the search are given in Table II.

V. SEARCHING O2 DATA

Most CW searches of LIGO data, including this one, begin with short Fourier Transforms (SFTs) of time segments of the data. Each SFT has duration $T_{\text{SFT}} = 1800$ s (see Appendix A). For each target, the first step is to compute the \mathcal{F} -statistic ‘atoms’, defined in Refs. [27, 84]. The data are split into $N_T = 23$ segments of duration $T_{\text{drift}} = 10$ d. The atoms are computed using the fixed values of RA and Dec in Table I, which are typically known for LMXBs.

A. Number of orbital templates

The next step is to define the search grid for each target in P , a_0 , and T_{asc} to compute the \mathcal{J} -statistic. It is

assumed that P , a_0 , and T_{asc} remain within the same bin throughout the search. When performing a gridded search, it is unlikely that the true signal parameters fall exactly on a grid point or template; there is some mismatch between the signal parameter and the template parameter. The grid is marked out so as to keep the mismatch to an acceptable level whilst keeping the number of templates low enough to be computationally feasible. We follow the same procedure as in Ref. [24]. Using Eq. (71) of Ref. [85], the number of P , a_0 , and T_{asc} templates are

$$N_P = \frac{\pi\sqrt{2}}{2} \mu_{\text{max}}^{-1/2} f a_0 \frac{\gamma T_{\text{drift}}}{\sqrt{12}} \frac{2\pi}{P^2} \Delta P, \quad (8)$$

$$N_{a_0} = \frac{\pi\sqrt{2}}{2} \mu_{\text{max}}^{-1/2} f \Delta a_0, \quad (9)$$

$$N_{T_{\text{asc}}} = \frac{\pi\sqrt{2}}{2} \mu_{\text{max}}^{-1/2} f a_0 \frac{2\pi}{P} \Delta T_{\text{asc}}, \quad (10)$$

where μ_{max} is the maximum allowed mismatch, which we choose to be 10% ($\mu_{\text{max}} = 0.1$) and γ is defined in general in Eq. (67) of Ref. [85]. The factor γ is a refinement factor introduced because the data are processed in 23 separate segments; in the special case of the O2 data considered here where the segments are contiguous in time, we have $\gamma = N_T = 23$ [85]. The values ΔP , Δa_0 , and ΔT_{asc} are the 3σ error bars on the EM measurements of P , a_0 , and T_{asc} respectively. We make a conservative estimate of N_P , N_{a_0} , and $N_{T_{\text{asc}}}$ by setting f equal to the largest frequency value in each sub-band. The grid is uniformly spaced in each sub-band.

For the five targets in this paper, we find $N_{a_0} < 1$ formally. Hence we search over P and T_{asc} with a_0 held fixed. In contrast, for the O2 search for Scorpius X-1, the frequency dependent number of templates ranges from $N_{a_0} = 768$ and $N_{T_{\text{asc}}} = 78$ for 60 Hz to $N_{a_0} = 8227$ and $N_{T_{\text{asc}}} = 824$ for 650 Hz [24]. For seven sub-bands, we find $N_P < 1$. The third and fourth columns of Table III show N_P and $N_{T_{\text{asc}}}$ respectively for each target and sub-band. Where Eq. 8 predicts an even number for N_P , we round up by one to ensure that the central value from EM observations is searched (e.g. where $N_P = 2$, we search $N_P = 3$). The fifth column shows the total number of templates $N_{\text{tot}} = N_P N_{a_0} N_{T_{\text{asc}}} = N_P N_{T_{\text{asc}}}$ for each target and sub-band.

B. Frequency binning

In Ref. [24], the search band is divided into equal sub-bands of width $\Delta f_{\text{band}} = 2^{20} \Delta f_{\text{drift}} = 0.6068148$ Hz. The choice of a power of two for $\Delta f_{\text{band}}/\Delta f_{\text{drift}}$ speeds up the computation of the Fourier transform [86]. We adopt the same binning strategy here². Every ten days

²The choice of sub-band varies between CW searches. An initial search for the Crab pulsar searched a range of 10^{-2} Hz around

TABLE II: Propagated time of ascension just before the start of O2, along with the error (in parentheses) and the search interval. The error in the second column is the 1σ uncertainty of the propagated T_{asc} except for XTE J1814-338, where it is the 90% interval. The search intervals in the third column are the $\pm 3\sigma$ range apart from XTE J0929-314. For XTE J0929-314, the search interval is equal to the orbital period, covering $T_{\text{asc}} \pm P/2$.

Target	$T_{\text{asc,O2}}$ (GPS time)	Search range (GPS time)
HETE J1900.1-2455	1 164 560 946(361)	1 164 559 863–1 164 562 029
IGR J00291+5934	1 164 557 364(96)	1 164 557 076–1 164 557 652
SAX J1808.4-3658	1 164 560 444(29)	1 164 560 357–1 164 560 531
XTE J0929-314	1 164 560 664(528)	1 164 559 356–1 164 561 973
XTE J1814-338	1 164 547 400(6)	1 164 547 382–1 164 547 418

TABLE III: Sub-band frequencies, number of templates and associated Gaussian and off-target Viterbi score thresholds. The second column shows the sub-band frequencies for $\{f_*/2, f_*, 4f_*/3, 2f_*\}$ where the value displayed is the start of the sub-band, which is ~ 0.61 Hz wide. For each sub-band, the third and fourth columns show the number of P and T_{asc} templates searched respectively (N_P and $N_{T_{\text{asc}}}$) (note: $N_{a_0} = 1$). The fifth column shows the total number of templates searched (N_{tot}). The final columns show the Viterbi score thresholds. The sixth column shows the Viterbi score threshold from identical searches on 100 synthetic Gaussian noise realisations S_{th}^G . The seventh column shows the Viterbi score threshold from identical searches on 100 randomly selected sky positions in real data $S_{\text{th}}^{\text{OT}}$. The thresholds are for a 0.30 false alarm probability per sub-band.

Target	Sub-band start frequency (Hz)	Number of templates			Threshold Viterbi score	
		N_P	$N_{T_{\text{asc}}}$	N_{tot}	S_{th}^G	$S_{\text{th}}^{\text{OT}}$
HETE J1900.1-2455	188.6	3	68	204	8.0	7.9
	377.0	3	135	405	8.2	8.2
	503.0	3	179	537	8.2	19.6
	754.4	5	268	1340	8.5	8.4
IGR J00291+5934	299.0	9	56	504	8.3	12.6
	598.4	17	113	1921	8.6	8.5
	798.2	21	151	3171	8.9	8.7
	1197.2	31	225	6975	9.1	8.9
SAX J1808.4-3658	200.0	3	14	42	7.5	7.4
	400.4	3	28	84	7.7	7.6
	534.2	5	37	185	7.9	7.9
	801.8	7	54	378	8.1	8.1
XTE J0929-314	92.0	1	26	26	7.4	7.2
	185.0	1	52	52	7.5	7.4
	246.8	1	70	70	7.6	7.6
	369.8	3	105	315	8.0	8.0
XTE J1814-338	156.8	1	8	8	6.9	6.9
	314.0	1	13	13	7.1	7.0
	419.0	1	17	17	7.2	7.2
	628.4	1	26	26	7.3	7.3

(i.e. T_{drift}), the frequency of the signal can increase or decrease by $\Delta f_{\text{drift}} = 5.787037 \times 10^{-7}$ Hz, or remain the same. For each target we search the ~ 0.61 Hz sub-bands which contain $f_*/2$, f_* , $4f_*/3$ and $2f_*$ (see Sec. IV). One advantage of the Viterbi algorithm is its speed, which allows us to search ~ 0.61 Hz cheaply. The sub-band boundaries are identical to those used in Ref. [24]; therefore the EM frequency may not be at the centre of the sub-band. There is no guarantee that the GW-emitting quadrupole and the X-ray emitting crust are exactly locked together; theoretical estimates of the balance between the nuclear pinning and Magnus forces in a neutron star predict a crust-core lag, for example [87, 88]. The starting frequencies of the sub-bands for each target are shown in the second column of Table III.

C. Thresholds

As described in Sec. IIB, the \mathcal{J} -statistic is applied to the SFTs to account for the Doppler modulation of the binary signal (Eq. 5) using the template defined by the orbital parameters P , a_0 , and T_{asc} . The Viterbi algorithm is then applied to find the best path through the 2^{20} frequency bins over $N_T = 23$ segments for each template.

The result of the search is a Viterbi score S , as described in Sec. IIA, corresponding to the most likely path for each orbital template (P , a_0 , T_{asc}) and sub-band. A path is a detection candidate if its Viterbi score exceeds a threshold S_{th} corresponding to a desired false alarm threshold. As the distribution of S in noise-only data is unknown analytically, Monte-Carlo simulations are used to establish S_{th} .

For our purposes, each sub-band is searched N_{tot} times as listed in Table III. The more templates are searched, the more likely that a single template results in an above-threshold score due solely to statistical fluctuation (i.e. a false alarm). The probability of experiencing a false alarm during a search is called the false alarm probability (FAP). The FAP can be defined as the probability of experiencing a false alarm when searching a single template (α), or the probability of a false alarm when searching all N_{tot} templates that constitute a search of a whole sub-band ($\alpha_{N_{\text{tot}}}$). For example, if we set $\alpha = 10^{-3}$ then the FAP of a sub-band amounts to $\approx 10^{-3}N_{\text{tot}}$ for $N_{\text{tot}} < 100$. The two probabilities α and $\alpha_{N_{\text{tot}}}$ are related by

$$\alpha_{N_{\text{tot}}} = 1 - (1 - \alpha)^{N_{\text{tot}}}. \quad (11)$$

We can therefore set $\alpha_{N_{\text{tot}}}$ and compute α .

Previous, comparable, CW searches for Scorpius X-1 have set the FAP per sub-band between 0.01 and 0.10, which yields an expected ~ 10 candidates across the full band spanning ~ 0.5 kHz and containing $\sim 10^2$ sub-bands [17, 21, 24]. In this paper, where we search only four sub-bands per independent target, it is arguably too conservative to set the FAP in the above range, especially

when one expects that any astrophysical signal lies near the detection limit of the experiment based on spin-down and torque-balance arguments (see Refs. [10, 15, 89, 90] and Sec. VIII). We therefore set $\alpha_{N_{\text{tot}}} = 0.30$ in the analysis which follows. Looking forward to the results in Sec. VII, it turns out that $\alpha_{N_{\text{tot}}} = 0.30$ yields ten above-threshold candidates in four of the targets, consistent with expectations, which are then screened by the vetoes in Sec. VI. Ten candidates is a modest number which keeps the veto workload manageable, while enhancing the chance of a detection. Naturally the reader is invited to set the FAP lower if desired. For example, if one sets the FAP to 0.10 per sub-band, the search yields zero above-threshold candidates across all five targets (see Sec. VII), again consistent with expectations.

It now remains to determine S_{th} , which we do in two ways: in synthetic Gaussian noise, and in real data to represent the detector noise more faithfully. We generate Gaussian noise realisations for each target and sub-band to calculate the Gaussian noise threshold S_{th}^{G} directly. The realisations are generated using the tool `lalapps_Makefakedata_v4` in the LIGO Scientific Collaboration Algorithm Library (LAL) [91]³. We use 100 realisations for each target and sub-band and the search is performed for each realisation. The $\alpha_{N_{\text{tot}}} = 0.30$ threshold from Gaussian noise realisations is shown in the sixth column of Table III for each target and sub-band. Typically S_{th}^{G} increases with N_{tot} , after allowing for statistical variations between sub-bands.

In reality, the LIGO noise is not Gaussian; it contains persistent harmonic features (lines). Some bands are particularly corrupted. In order to correct for this, we also perform the search at each P , a_0 , and T_{asc} template and sub-band for 100 random off-target sky positions (varying RA and Dec) using the real O2 data. The off-target thresholds per sub-band $S_{\text{th}}^{\text{OT}}$ are higher than the Gaussian thresholds, if the sub-band is noisy. The results for $\alpha_{N_{\text{tot}}} = 0.30$ are shown in the seventh column of Table III. The scores in columns six and seven are rounded down to one decimal place to avoid rejecting marginal templates due to rounding errors. We see that there is little difference between S_{th}^{G} and $S_{\text{th}}^{\text{OT}}$ except in the 503.0 Hz and 299.0 Hz sub-bands which contain known instrumental artefacts.

VI. VETOES

Templates may produce Viterbi scores above the thresholds defined in Sec. VC. We examine whether there are reasonable grounds to systematically veto these candidates as non-astrophysical sources. In Sec. VIA we lay out the veto criteria following the method and notation

³In the O2 Scorpius X-1 search [24], realisations were computed in seven sub-bands covering 60–650 Hz, and S_{th} was extrapolated for computational efficiency.

of Ref. [24]. Four vetoes are copied from Refs. [21, 24]. The off-target veto is new for this paper. In Sec. **VIB** we explain how to classify the results of vetos 2 and 3.

A. Veto descriptions

1. Known lines

The detector output contains many harmonic features (instrumental lines), which have been identified as noise as part of the detector characterisation process [92]. The physical sources of these noise lines are varied. Sometimes the effect can be mitigated, but not always.

A candidate in proximity to a known noise line [93] at frequency f_{line} is vetoed, if the optimal HMM path $f_{\cup}(t)$ satisfies $|f_{\cup}(t) - f_{\text{line}}| < 2\pi a_0 f_{\cup}(t)/P$ for any t in the range $0 \leq t \leq T_{\text{obs}}$.

2. Single interferometer

The second veto is applied by searching the data from each interferometer separately. If a signal is astrophysical in origin, and if it is relatively strong, it should be found in the analysis of both detectors individually. If an astrophysical signal is relatively weak, it may be found in neither detector individually, even though it is found in the combined data. The interpretation of the Viterbi scores for single interferometer vetoes are described in Sec. **VIB**.

3. $T_{\text{obs}}/2$

The third veto is applied by splitting the data in two segments and searching the two intervals separately. Again, if the signal is astrophysical and strong, it should be present in both halves of the data. If the signal is weak it may be below the threshold in both halves.

The O2 data are split so that the first segment covers 140 days and the second 90 days. This division is copied from Ref. [24] and is chosen so that the effective observing time (accounting for the duty cycle of the interferometers) is approximately equal in the two segments.

As with the single interferometer veto, the interpretation of Viterbi scores from the $T_{\text{obs}}/2$ veto is described in Sec. **VIB**.

4. Off target search

The fourth veto, which is new (cf. Refs. [21] and [24]), is applied by searching in an off-target sky position. If the off-target search returns a score above threshold, the origin of the signal is likely to be instrumental. In this paper off-target means the position of the target plus 10 m and plus 10' for RA and Dec respectively.

5. T_{drift}

The last veto is applied by analysing the frequency wandering of the Viterbi path [21]. A signal whose wandering timescale exceeds T_{drift} should return a higher S , when T_{drift} is increased to the observed wandering time-scale. This veto cannot be applied if the wandering timescale is already close to T_{drift} , which is the case in Ref. [24] and also for this search (see Sec. **VII** and Appendix **B**).

B. Veto scenarios

The interpretation of the Viterbi scores under the single interferometer and $T_{\text{obs}}/2$ vetoes divides into four scenarios as in Ref. [24]. We label the original score by S_{\cup} , the threshold score (see Sec. **VC**) by S_{th} , and the two veto runs by S_{a} and S_{b} , i.e. the scores from two individual detectors or from the two halves of the data.

Category A. One veto search returns a sub-threshold score whilst the other is higher than the original search:

$$(S_{\text{a}} < S_{\text{th}}) \wedge (S_{\text{b}} > S_{\cup}), \quad (12)$$

where \wedge denotes Boolean AND. If the frequency f_{b} associated with S_{b} is close to that of the original candidate f_{\cup} ,

$$|f_{\cup} - f_{\text{b}}| < 2\pi a_0 f_{\cup}/P, \quad (13)$$

then we conclude that the signal is likely to be a noise artefact in one detector or one half of the data. Category A candidates are vetoed.

Category B. The situation is identical to Category A, except that the paths are not close, with $|f_{\cup} - f_{\text{b}}| > 2\pi a_0 f_{\cup}/P$. The two veto searches may not have found the same signal in both detectors or halves of the data. This could be due to the search instead finding a noise artefact in one detector or half the data. Perhaps the signal is too weak to be detected in only one interferometer or half the data. Category B candidates cannot be vetoed.

Category C. The candidate exceeds the threshold in both veto searches:

$$(S_{\text{a}} > S_{\text{th}}) \wedge (S_{\text{b}} > S_{\text{th}}). \quad (14)$$

This could represent a strong astrophysical signal. Equally it could represent a noise source which is common to both detectors or present in the full observing run. Category C candidates cannot be vetoed.

Category D. The candidate falls below the threshold in both veto searches:

$$(S_{\text{a}} < S_{\text{th}}) \wedge (S_{\text{b}} < S_{\cup}). \quad (15)$$

The origin of the combined detection is unclear. One possibility is that it is a weak astrophysical signal which requires the full data set to be detectable. Category D candidates cannot be vetoed.

VII. O2 SEARCH RESULTS

In this section we present search results for the five LMXB targets listed in Table I. Ten templates have scores exceeding the $\alpha_{N_{\text{tot}}} = 0.30$ thresholds set in Sec. VC. Of these: four have scores above both thresholds (i.e. $S_{\text{U}} > S_{\text{th}}^{\text{G}}$ and $S_{\text{U}} > S_{\text{th}}^{\text{OT}}$), three have $S_{\text{U}} > S_{\text{th}}^{\text{G}}$ only, and three have $S_{\text{U}} > S_{\text{th}}^{\text{OT}}$ only. We apply the veto procedure outlined in Sec. VI to the ten candidates. There are two further templates which have scores within 0.4% of $S_{\text{th}}^{\text{OT}}$ (see Figs. 5 and 7 in Appendix B). No other templates are within 1.8% of $S_{\text{th}}^{\text{OT}}$. For completeness we add these nearly above-threshold templates as candidates to be considered by the veto procedure, although note they do not meet our formal $\alpha_{N_{\text{tot}}} = 0.30$ FAP target. There are similarly close templates to S_{th}^{G} in two other sub-bands (503.0 Hz and 299.0 Hz for HETE J1900.1-2455 and IGR J00291+5934 respectively). We do not include these in the veto procedure due to the presence of broad instrumental lines in these sub-bands (see Fig. 2 and Fig. 5 in Appendix B). We follow up 12 templates in total (ten above-threshold and two nearly above-threshold).

The Viterbi scores and frequencies of the candidates are summarized in Fig. 1. Each marker shows the terminating frequency of a candidate's Viterbi path (i.e. q^* as defined in Sec. IIA) and the associated Viterbi score. Candidates for each target are shown by different marker shapes. The ten above-threshold candidates and two nearly above-threshold templates are shown in orange and blue respectively. Candidates which are removed through the veto procedure are indicated by the black-square and black-circle outlines for elimination by veto 1 and veto 3 respectively.

The FAP per sub-band in this paper is deliberately set higher than in previous, comparable, CW searches for Scorpius X-1, because the total number of sub-bands is lower, as noted in Sec. VC. If we set the FAP per sub-band to 0.20 instead of 0.30, all candidates except three fall below the Gaussian and off-target thresholds and do not graduate to the veto stage. One of these candidates is the highest scoring template in the IGR J00291+5934 $f_{\star}/2$ sub-band ($S_{\text{U}} \approx 8.5$), which is eliminated by veto 1. The other two candidates are the two highest scoring templates in the HETE J1900.1-2455 $2f_{\star}$ sub-band ($S_{\text{U}} \approx 8.5$ and $S_{\text{U}} \approx 8.8$) which survive the veto procedure. If we set the FAP per sub-band to 0.10 instead of 0.30, zero candidates exceed the Gaussian and off-target thresholds. The reader is invited to experiment with various choices of FAP when reproducing the results.

The search uses a combination of central processing unit (CPU) and graphical processing unit (GPU) computation. We work with a GPU implementation of the \mathcal{J} -statistic identical to the one in Ref. [24]. We use the computing facilities of the OzSTAR supercomputer [94]. OzSTAR has compute nodes with Xeon Gold 6140 CPUs running at 2.3 GHz [95] and NVIDIA P100 12GB PCIe

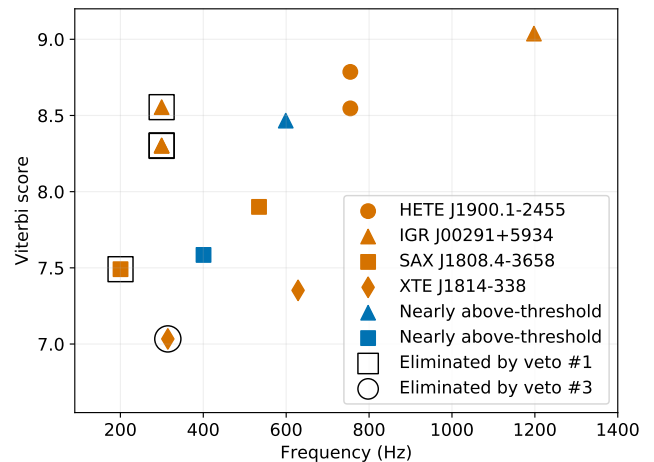


FIG. 1: Summarized search results for all LMXB targets. The horizontal axis shows the frequency at the end of the best path for the template and the vertical axis shows the associated Viterbi score. Each orange marker indicates a template which has resulted in a path with a Viterbi score higher than either of the Gaussian or off-target thresholds or both. Results for HETE J1900.1-2455, IGR J00291+5934, SAX J1808.4-3658, and XTE J1814-338 are shown by the circle, triangle, square, and diamond markers respectively. There are no above-threshold candidates for XTE J0929-314. The additional blue markers for IGR J00291+5934 and SAX J1808.4-3658 (at ~ 400 Hz and ~ 600 Hz respectively) indicate templates with $S_{\text{U}} \approx S_{\text{th}}^{\text{OT}}$ which are included for safety in the face of rounding errors. Candidates outlined with a black square or circle indicate templates vetoed by veto 1 (known lines) and veto 3 ($T_{\text{obs}}/2$) respectively. We note that there are two almost identical IGR J00291+5934 markers at $S_{\text{U}} \approx 8.3$, $f \approx 300$ Hz (indistinguishable in the figure). Both are eliminated by veto 1.

GPU cards benchmarked at ≈ 9.3 TeraFLOPS (floating point operations per second) single-precision performance [96]. On OzSTAR the search takes ≈ 5 CPU-hours and ≈ 23 GPU-hours (every GPU-hour also requires one CPU-hour). The false alarm thresholds take ≈ 1000 CPU-hours and ≈ 4600 GPU-hours to perform 100 searches on Gaussian and real data off-target realisations.

In sections VII A–VII E we summarize the search results for each of the five targets. The results are laid out in full in Fig. 2 for one target only, namely HETE J1900.1-2455, to guide the reader without cluttering the main body of the paper. The complete search results, including veto outcomes and optimal Viterbi paths are collated for reference and reproducibility in Appendix B. The O2 search returns five veto survivors. A search of

LIGO O1 data narrowly targeted at the templates in the sub-bands containing the five veto survivors shows no support for an astrophysical signal.

A. HETE J1900.1-2455

The search for HETE J1900.1-2455 returns two candidates as shown in Fig. 2. Each marker in Fig. 2 shows the terminating frequency of the best path for a template and associated Viterbi score. The vertical red-dot-dash and green-dash lines show the S_{th}^{G} and $S_{\text{th}}^{\text{OT}}$ thresholds respectively (for $\alpha_{N_{\text{tot}}} = 0.30$). A marker with a higher Viterbi score than the threshold lines indicates an above-threshold candidate. The four panels in Fig. 2 show the search results in each sub-band: $f_*/2$ (top-left), f_* (top-right), $4f_*/3$ (bottom-left), and $2f_*$ (bottom-right). There are two candidates in the $2f_*$ sub-band and zero candidates in the other three sub-bands. The $4f_*/3$ sub-band is noisy. The horizontal line and shaded bands in the bottom-left panel show where there are instrumental lines. The solid line indicates the peak of the instrumental line and the transparent shading shows its extent (see Refs. [92, 93]). Instrumental lines in the Hanford and Livingston data are shown in orange and blue respectively. The instrumental lines in the $4f_*/3$ sub-band are due to violin modes of the Hanford and Livingston detectors. The Hanford line peaks at 503.11 Hz with a range 503.10–503.13 Hz and the Livingston line peaks at 503.1825 Hz with range 502.9500–503.3000 Hz (covering the entire plotted region)[93].

The candidates in the $2f_*$ sub-band are above both S_{th}^{G} and $S_{\text{th}}^{\text{OT}}$. Both candidates survive vetoes 1, 2, 3, and 4. Veto 5 is not applicable as the frequency wandering timescales of the candidate paths is $\approx T_{\text{drift}}$ (see Fig. 4 in Appendix B). The frequency paths, Viterbi scores, and veto outcomes for these candidates are further detailed in Appendix B.

B. IGR J00291+5934

The search for IGR J00291+5934 returns four candidates. Three are above S_{th}^{G} and one is above $S_{\text{th}}^{\text{OT}}$ (zero of these are above both thresholds). We include a fifth nearly above-threshold template in the veto procedure due to its proximity to $S_{\text{th}}^{\text{OT}}$ in the face of rounding errors. The search results, frequency paths, and veto outcomes are shown in Appendix B (Fig. 5, Fig. 6, and Table VI respectively).

Three of the candidate are in the $f_*/2$ sub-band. They have scores which are above S_{th}^{G} and below $S_{\text{th}}^{\text{OT}}$. All three candidates are eliminated by veto 1 due to a broad instrumental line in the Hanford data (see Fig. 5 in Appendix B). The other above-threshold candidate is in the $2f_*$ sub-band with $S_{\text{U}} > S_{\text{th}}^{\text{OT}}$ and $S_{\text{U}} < S_{\text{th}}^{\text{G}}$. It survives vetoes 1–4. Veto 5 is not applicable. The nearly above-threshold template is in the f_* sub-band. It survives

vetoes 1–4 and veto 5 is not applicable.

C. SAX J1808.4-3658

The search for SAX J1808.4-3658 finds two candidates. A third template almost equals the threshold, and we include it in the veto procedure. See Appendix B for full search results, candidate frequency paths, and veto outcomes.

One candidate is in the $f_*/2$ sub-band with $S_{\text{U}} < S_{\text{th}}^{\text{G}}$ and $S_{\text{U}} > S_{\text{th}}^{\text{OT}}$. It is eliminated by veto 1 due to proximity to an instrumental line in the Livingston data (see Fig. 7 in Appendix B). There is one candidate in the $4f_*/3$ sub-band. It is close to, but just above both thresholds ($S_{\text{U}} \gtrsim S_{\text{th}}^{\text{G}}$ and $S_{\text{U}} \gtrsim S_{\text{th}}^{\text{OT}}$). The candidate survives vetoes 1–4 and veto 5 is not applicable. The nearly above-threshold template is in the f_* sub-band with $S_{\text{U}} \approx S_{\text{th}}^{\text{OT}}$. It survives vetoes 1–4 and veto 5 is not applicable.

D. XTE J0929-314

The search for XTE J0929-314 returns zero candidates with $S_{\text{U}} > S_{\text{th}}^{\text{G}}$ or $S_{\text{U}} > S_{\text{th}}^{\text{OT}}$. Full search results for XTE J0929-314 are shown in Fig. 9 in Appendix B.

E. XTE J1814-338

The XTE J1814-338 search returns two candidates. One candidate is in the f_* sub-band with $S_{\text{U}} < S_{\text{th}}^{\text{G}}$ and $S_{\text{U}} > S_{\text{th}}^{\text{OT}}$. It survives vetoes 1 and 2. It is eliminated by veto 3 as the signal is found to be stronger in the later part of O2. The other candidate, in the $2f_*$ sub-band, scores above both thresholds. It survives vetoes 1–4. Veto 5 is not applicable. See Appendix B for full search results.

VIII. EXPECTED GW STRAIN FROM LMXBS

In view of the results in Sec. VII, it is useful to ask how strong the signal from a particular source is expected to be, given the EM information available. From Eq. (52) in Ref. [10], the indirect spin-down limit on the maximum GW strain $h_{0,\text{sd}}$ is

$$h_{0,\text{sd}} = 2.5 \times 10^{-25} \left(\frac{1 \text{ kpc}}{D} \right) \times \left[\left(\frac{1 \text{ kHz}}{f_{\text{gw}}} \right) \left(\frac{-\dot{f}_{\text{gw}}}{10^{-10} \text{ Hz s}^{-1}} \right) \left(\frac{I_{zz}}{I_0} \right) \right]^{1/2}, \quad (16)$$

where f_{gw} and \dot{f}_{gw} are the GW frequency and frequency derivative respectively, D is the distance to the source, I_{zz} is the zz component of the moment-of-inertia tensor,

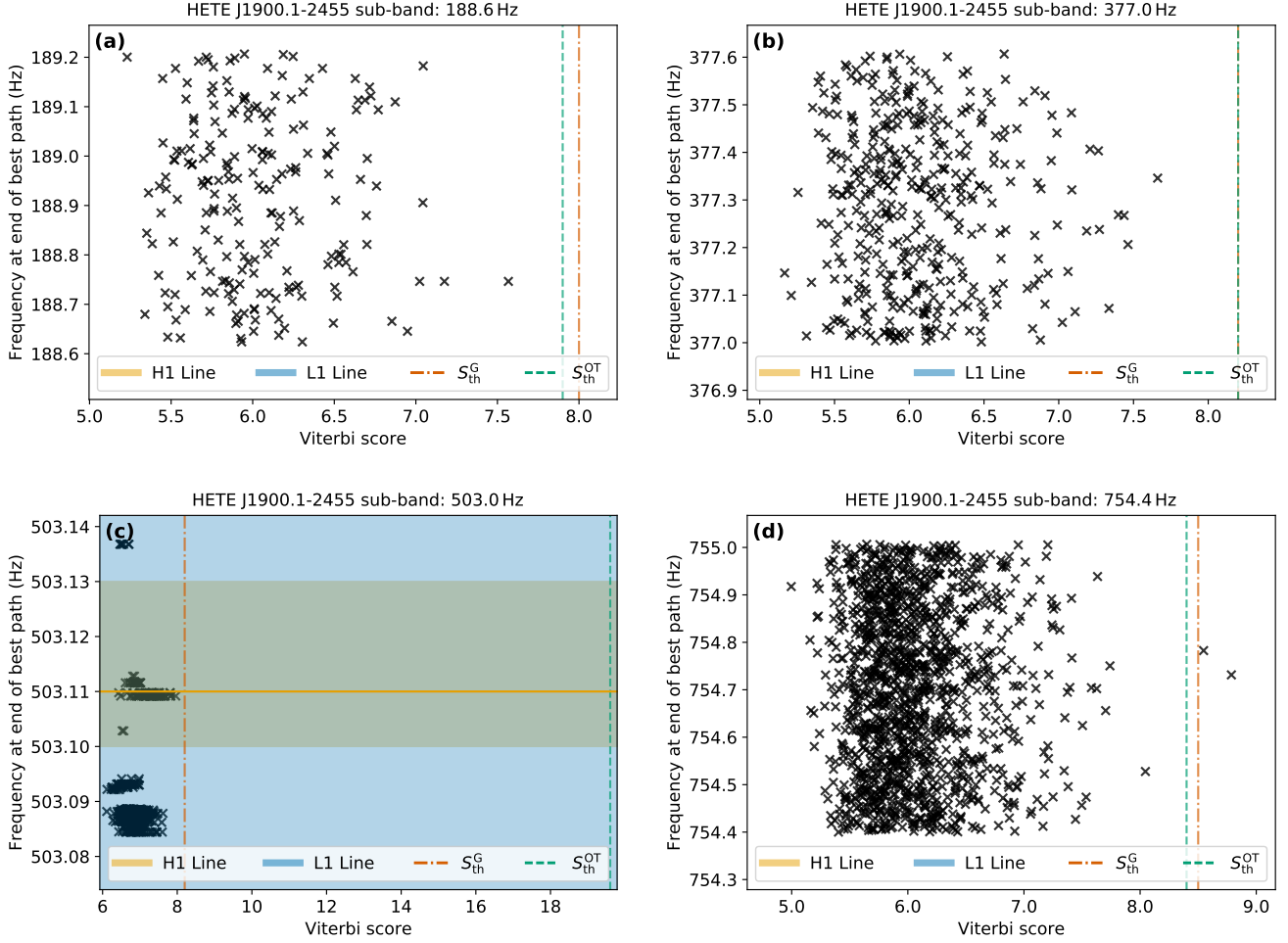


FIG. 2: Search results for HETE J1900.1-2455 at the four sub-bands corresponding to $f_*/2$, f_* , $4f_*/3$, and $2f_*$ in panels (a), (b), (c), and (d) respectively. Each point marks the terminating frequency of the best path for a template (vertical axis) and the associated Viterbi score (horizontal axis). The vertical lines indicate S_{th} for a false alarm probability of 0.30 per sub-band determined from 100 Gaussian noise realisations S_{th}^{G} (red-dot-dash) and 100 off-target searches $S_{\text{th}}^{\text{OT}}$ (green-dash). The orange and blue horizontal stripes indicate known instrumental lines in the Hanford and Livingston observatories respectively; the solid-line indicates where the instrumental line peaks and the shading indicates its width. In the case of the sub-band starting at 503.0 Hz, broad instrumental lines cover the whole frequency range of the plot. Where there is a loud instrumental line in a sub-band, the search is likely to select paths very close to the instrumental line. This means that the paths for a contaminated sub-band can lie entirely within the instrumental line. The instrumental lines in sub-band 503.0 Hz are due to violin mode resonances in the detector mirror suspensions [93]. There are two candidates above both S_{th}^{G} and $S_{\text{th}}^{\text{OT}}$ in the $2f_*$ sub-band (bottom-right). Similar plots for the other four targets can be found in Appendix B.

and I_0 is the moment of inertia of the un-deformed star. For our purposes, we make the assumptions $I_{zz}/I_0 \approx 1$, $f_{\text{gw}} \propto f_*$, and $\dot{f}_{\text{gw}} \propto \dot{f}_*$.

As described in Sec. III, EM observations constrain f_* and \dot{f}_* during both active and quiescent phases. Many of our targets have a range of estimates from observations of different phases. During active periods, the neutron star typically spins up, although this is not always the case; the hydromagnetic accretion torque can be negative [38]. In quiescence, the neutron star typically spins down.

In Table IV, we collate estimates of \dot{f}_* for each of the targets. IGR J00291+5934 and SAX J1808.4-3658 have several values of \dot{f}_* estimated from observations of different active and quiescent phases. These two targets both follow the typical picture of active spin up ($f_{\text{act}} > 0$) and quiescent spin down ($f_{\text{qu}} < 0$). XTE J0929-314 and XTE J1814-338 have only a single observed active phase and therefore each have only one \dot{f}_* estimate. Both exhibit active spin down, unlike IGR J00291+5934 and SAX J1808.4-3658 which show active spin up. HETE

TABLE IV: Spin-down limits on the maximum GW strain inferred from EM observations for IGR J00291+5934, SAX J1808.4-3658, XTE J0929-314 and XTE J1814-338 (HETE J1900.1-2455 is excluded as there is no frequency derivative measurement). The first column summarizes the target name and estimated distance D . The second column indicates whether the \dot{f}_\star observation is from an active or quiescent phase. The third and fourth columns show the observed frequency derivative \dot{f}_\star and the associated spin-down limit $h_{0,\text{sd}}$ respectively using the minimum D from the first column. The final two columns reference the data used for the estimate. The $h_{0,\text{sd}}$ limits marked with * indicate $\dot{f}_{\text{act}} > 0$ where the assumption $\dot{f}_{\text{gw}} \approx -\dot{f}_{\text{act}}$ is made.

Target Details	Active or quiescent	Freq. derivative \dot{f} (Hz s $^{-1}$)	Spin-down limit $h_{0,\text{sd}}$	Notes	Ref.
IGR J00291+5934 $4 < D/\text{kpc} < 6$ [61, 62]	Quiescent	$-4.1(1.4) \times 10^{-15}$	5.2×10^{-28}	Before 2008 outburst	[67]
	Active	$+3(5) \times 10^{-12}$	$1.4 \times 10^{-26*}$	2015 outburst	[50]
	Active	$+5.1(4) \times 10^{-15}$	$5.8 \times 10^{-28*}$	2008 outburst	[67]
SAX J1808.4-3658 $D \approx 3.4\text{--}3.6$ kpc [69]	Quiescent	$-5.5(1.2) \times 10^{-16}$	2.7×10^{-28}	Five outbursts up to 2008	[97]
	Quiescent	$-1.65(20) \times 10^{-15}$	4.7×10^{-28}	Six outbursts up to 2011	[98]
	Active	$+2.6(3) \times 10^{-11}$	$5.9 \times 10^{-26*}$	2015 outburst (XMM-Newton data)	[53]
	Active	$+1.1(3) \times 10^{-10}$	$1.2 \times 10^{-25*}$	2015 outburst (NuSTAR data)	[53]
	Quiescent	$-1.5(2) \times 10^{-15}$	4.5×10^{-28}	Long-term spin-down	[53]
XTE J0929-314 $D > 7.4$ kpc [71]	Active	$-9.2(4) \times 10^{-14}$	2.4×10^{-27}	2002 outburst	[54]
XTE J1814-338 $D \approx 3.8\text{--}8$ kpc [73, 74]	Active	$-6.7(7) \times 10^{-14}$	3.0×10^{-27}	2003 outburst	[48]

J1900.1-2455 is excluded from this calculation, as there is no \dot{f}_\star measurement from the short time it exhibited pulsations.

Many of the targets have a range of D estimates, which we summarize in the first column of Table IV. To calculate the maximum $h_{0,\text{sd}}$, we use the minimum D for each target.

For $\dot{f}_\star < 0$, we compute $h_{0,\text{sd}}$ assuming $\dot{f}_{\text{gw}} \approx \dot{f}_\star$. The $h_{0,\text{sd}}$ estimates are collected in the fourth column of Table IV. We find that the maximum $h_{0,\text{sd}}$ for $\dot{f}_\star < 0$ comes from the active phases of XTE J0929-314 and XTE J1814-338 with $h_{0,\text{sd}} \lesssim 2.4 \times 10^{-27}$ and $\lesssim 3.0 \times 10^{-27}$ respectively. For comparison, the Scorpius X-1 O2 search set an upper limit on the detectable wave strain of 3.47×10^{-25} at 194.6 Hz with 95% confidence [24].

Equation 16 requires $\dot{f}_\star < 0$. For $\dot{f}_\star > 0$, we can make a different order of magnitude estimate for $h_{0,\text{sd}}$. When the star is observed to spin up, the positive net torque (dominated by accretion) may mask a negative gravitational radiation reaction torque of a similar order of magnitude. In principle, $\dot{f}_{\text{act}} > 0$ allows for an arbitrarily large frequency derivative due to accretion, i.e. $\dot{f}_{\text{acc}} > 0$ can be as large as one wishes, as long as we also have $|\dot{f}_{\text{gw}}| = \dot{f}_{\text{acc}} - \dot{f}_{\text{act}}$. One arguably plausible scenario, without excessive fine tuning, is $\dot{f}_{\text{act}} \sim \dot{f}_{\text{acc}} \sim |\dot{f}_{\text{gw}}|$. On

the other hand, for $\dot{f}_{\text{act}} = \dot{f}_{\text{acc}} - |\dot{f}_{\text{gw}}| < 0$, one must have $|\dot{f}_{\text{gw}}| \geq \dot{f}_{\text{act}}$, and setting $|\dot{f}_{\text{gw}}| = \dot{f}_{\text{act}}$ yields a conservative bound. For the observations with $\dot{f}_\star \geq 0$, we therefore estimate $h_{0,\text{sd}}$ assuming $\dot{f}_{\text{gw}} = -\dot{f}_\star$. We find $h_{0,\text{sd}}$ in the range 10^{-28} to 10^{-25} for the active phases of IGR J00291+5934 and SAX J1808.4-3658. None of the targets were active during O2.

We can also calculate the maximum signal strength based on the observed X-ray flux assuming that the accretion and gravitational radiation reaction torques balance each other. The torque-balance limit is [10, 15, 89, 90],

$$h_{\text{torque}} = 5 \times 10^{-27} \times \sqrt{\left(\frac{600 \text{ Hz}}{f_{\text{gw}}}\right) \left(\frac{F_{\text{X}}}{10^{-8} \text{ erg cm}^{-2} \text{ s}^{-1}}\right)}, \quad (17)$$

where F_{X} is the X-ray flux. In the second and third column of Table V we list the long-term flux from Table 1 of Ref. [36] and the maximum flux from the LMXB catalogue in Ref. [99] respectively. The third column shows the range of h_{torque} given these values. For some of the targets, the h_{torque} limits are lower than the $h_{0,\text{sd}}$ limits in Table IV during active phases. However the numbers are comparable to $h_{0,\text{sd}}$ in quiescence.

TABLE V: Torque-balance limit h_{torque} on the GW strain based on EM observations. The second column is the long-term X-ray flux from table 1 of Ref. [36]; see also references therein. The third column is the maximum flux from the LMXB catalogue in Ref. [99]. The final column shows the estimated range of h_{torque} for the listed fluxes calculated using $f_{\text{gw}} = 2f_{\star}$ in Eq. 17.

Target	Flux ($\times 10^{-8} \text{erg cm}^{-2} \text{s}^{-1}$)		h_{torque} ($\times 10^{-27}$)
	Long-term	Maximum	
HETE J1900.1-2455	0.18	0.238	1.9–2.2
IGR J00291+5934	0.018	0.281	0.5–1.9
SAX J1808.4-3658	0.086	0.211	1.3–2.0
XTE J0929-314	0.027	0.069	1.0–1.7
XTE J1814-338	0.013	0.025	0.6–0.8

IX. CONCLUSIONS

In this paper we present results of a search for continuous gravitational waves from five LMXBs in the LIGO O2 dataset. The search uses a hidden Markov model to track spin wandering and the \mathcal{J} -statistic matched filter to track orbital phase. The LMXBs have electromagnetically measured pulsation frequencies, thereby restricting the parameter space relative to searches for other objects like Scorpius X-1 [16, 21, 23, 24]. A Gaussian threshold is set using searches on 100 realisations of Gaussian noise. An off-target threshold is set by searching the O2 dataset in 100 random off-target sky positions.

We find no candidates above a threshold corresponding to a 0.10 FAP per sub-band. We find ten candidates above a threshold corresponding to a 0.30 FAP per sub-band. After applying vetoes we are left with five candidates (two for HETE J1900.1-2455 and one each for IGR J00291+5934, SAX J1808.4-3658, and XTE J1814-338). The survivors are marginally above the $\alpha_{N_{\text{tot}}} = 0.30$

threshold, exceeding it by less than ≈ 0.4 in Viterbi score. The number of survivors is statistically consistent with the number of false alarms expected from a FAP of 0.30 per sub-band for 20 sub-bands (i.e. $0.30 \times 20 = 6$).

It is premature to speculate about the nature of the surviving candidates. We recommend that they be followed up in future observations, including LIGO-Virgo Observing Run 3.

ACKNOWLEDGEMENTS

The authors are grateful to Sofia Suvorova, William Moran, and Robin Evans for their past developmental work on HMMs for continuous wave searches and also to them and Margaret Millhouse, Patrick Meyers, and Julian Carlin for helpful discussions including advice on the off-target threshold and veto procedure; Shanika Galaudage and Duncan Galloway for advice on selecting LMXB targets and locating the most accurate EM measurements of the targets' parameters in the literature; and Ling Sun for helpful comments on the manuscript. We also thank the Continuous Wave Working Group of the LIGO Scientific Collaboration and Virgo Collaboration for their useful discussion. This research is supported by the Australian Research Council Centre of Excellence for Gravitational Wave Discovery (OzGrav) (project number CE170100004). This work used computational resources of the OzSTAR national facility at Swinburne University of Technology and also at the California Institute of Technology. OzSTAR is funded by Swinburne University of Technology and the National Collaborative Research Infrastructure Strategy (NCRIS). This research has made use of data, software and/or web tools obtained from the Gravitational Wave Open Science Center (<https://www.gw-openscience.org>), a service of LIGO Laboratory, the LIGO Scientific Collaboration and the Virgo Collaboration. LIGO is funded by the U.S. National Science Foundation. Virgo is funded by the French Centre National de Recherche Scientifique (CNRS), the Italian Istituto Nazionale della Fisica Nucleare (INFN) and the Dutch Nikhef, with contributions by Polish and Hungarian institutes. This work has been assigned LIGO document number P1900273.

-
- [1] LIGO Scientific Collaboration, J. Aasi, B. P. Abbott, et al. Advanced LIGO. *Classical and Quantum Gravity*, 32:074001, Apr 2015.
 - [2] F. Acernese, M. Agathos, K. Agatsuma, et al. Advanced Virgo: a second-generation interferometric gravitational wave detector. *Classical and Quantum Gravity*, 32:024001, Jan 2015.
 - [3] B. P. Abbott, R. Abbott, T. D. Abbott, et al.
 - [4] B. P. Abbott, R. Abbott, T. D. Abbott, et al. GW151226: Observation of Gravitational Waves from a 22-Solar-Mass Binary Black Hole Coalescence. *Phys. Rev. Lett.*, 116(24):241103, June 2016.
 - [5] B. P. Abbott, R. Abbott, T. D. Abbott, et al. GW170104: Observation of a 50-Solar-Mass Binary Black Hole Coalescence at Redshift 0.2. *Phys. Rev. Lett.*, 118(22):221101, June 2017.
 - [6] B. P. Abbott, R. Abbott, T. D. Abbott, et al. GW170814: A Three-Detector Observation of Gravitational Waves from a Binary Black Hole Coalescence. *Phys. Rev. Lett.*, 119(14):141101, October 2017.
 - [7] B. P. Abbott, R. Abbott, T. D. Abbott, et al. GWTC-1: A Gravitational-Wave Transient Catalog of Compact

- Binary Mergers Observed by LIGO and Virgo during the First and Second Observing Runs. *Physical Review X*, 9(3):031040, July 2019.
- [8] B. P. Abbott, R. Abbott, T. D. Abbott, et al. GW170817: Observation of Gravitational Waves from a Binary Neutron Star Inspiral. *Phys. Rev. Lett.*, 119(16):161101, October 2017.
- [9] B. P. Abbott, R. Abbott, T. D. Abbott, et al. Multi-messenger Observations of a Binary Neutron Star Merger. *Astrophysical Journal, Letters*, 848(2):L12, October 2017.
- [10] K. Riles. Gravitational waves: Sources, detectors and searches. *Progress in Particle and Nuclear Physics*, 68:1–54, Jan 2013.
- [11] N. Andersson, V. Ferrari, D. I. Jones, et al. Gravitational waves from neutron stars: promises and challenges. *General Relativity and Gravitation*, 43(2):409–436, Feb 2011.
- [12] W. H. G. Lewin, J. van Paradijs, and E. P. J. van den Heuvel. *X-ray Binaries*. January 1997.
- [13] Walter H. G. Lewin and Michiel van der Klis. *Compact Stellar X-ray Sources*, volume 39. 2006.
- [14] Jorge Casares, Peter Gustaaf Jonker, and Garik Israelian. *X-Ray Binaries*, page 1499. 2017.
- [15] Lars Bildsten. Gravitational Radiation and Rotation of Accreting Neutron Stars. *Astrophysical Journal, Letters*, 501(1):L89–L93, Jul 1998.
- [16] B. Abbott, R. Abbott, R. Adhikari, et al. Searches for periodic gravitational waves from unknown isolated sources and Scorpius X-1: Results from the second LIGO science run. *Phys. Rev. D*, 76(8):082001, Oct 2007.
- [17] J. Aasi, B. P. Abbott, R. Abbott, et al. Directed search for gravitational waves from Scorpius X-1 with initial LIGO data. *Phys. Rev. D*, 91(6):062008, Mar 2015.
- [18] J. Aasi, B. P. Abbott, R. Abbott, et al. First all-sky search for continuous gravitational waves from unknown sources in binary systems. *Phys. Rev. D*, 90(6):062010, Sep 2014.
- [19] J. Abadie, B. P. Abbott, R. Abbott, et al. Directional Limits on Persistent Gravitational Waves Using LIGO S5 Science Data. *Phys. Rev. Lett.*, 107(27):271102, Dec 2011.
- [20] G. D. Meadors, E. Goetz, K. Riles, T. Creighton, and F. Robinet. Searches for continuous gravitational waves from Scorpius X-1 and XTE J1751-305 in LIGO’s sixth science run. *Phys. Rev. D*, 95(4):042005, Feb 2017.
- [21] B. P. Abbott, R. Abbott, T. D. Abbott, et al. Search for gravitational waves from Scorpius X-1 in the first Advanced LIGO observing run with a hidden Markov model. *Phys. Rev. D*, 95(12):122003, Jun 2017.
- [22] B. P. Abbott, R. Abbott, T. D. Abbott, et al. Directional Limits on Persistent Gravitational Waves from Advanced LIGO’s First Observing Run. *Phys. Rev. Lett.*, 118(12):121102, Mar 2017.
- [23] B. P. Abbott, R. Abbott, T. D. Abbott, et al. Upper Limits on Gravitational Waves from Scorpius X-1 from a Model-based Cross-correlation Search in Advanced LIGO Data. *Astrophys. J.*, 847(1):47, Sep 2017.
- [24] B. P. Abbott, R. Abbott, T. D. Abbott, et al. Search for gravitational waves from Scorpius X-1 in the second Advanced LIGO observing run with an improved hidden Markov model. *Phys. Rev. D*, 100(12):122002, December 2019.
- [25] B. P. Abbott, R. Abbott, T. D. Abbott, et al. Directional limits on persistent gravitational waves using data from advanced ligo’s first two observing runs. *Phys. Rev. D*, 100:062001, Sep 2019.
- [26] Grant David Meadors, Badri Krishnan, Maria Alessandra Papa, John T. Whelan, and Yuanhao Zhang. Resampling to accelerate cross-correlation searches for continuous gravitational waves from binary systems. *Phys. Rev. D*, 97(4):044017, February 2018.
- [27] S. Suvorova, P. Clearwater, A. Melatos, et al. Hidden Markov model tracking of continuous gravitational waves from a binary neutron star with wandering spin. II. Binary orbital phase tracking. *Phys. Rev. D*, 96(10):102006, November 2017.
- [28] S. Suvorova, L. Sun, A. Melatos, W. Moran, and R. J. Evans. Hidden Markov model tracking of continuous gravitational waves from a neutron star with wandering spin. *Phys. Rev. D*, 93(12):123009, June 2016.
- [29] L. Wang, D. Steeghs, D. K. Galloway, T. Marsh, and J. Casares. Precision Ephemerides for Gravitational-wave Searches - III. Revised system parameters of Sco X-1. *Monthly Notices of the RAS*, 478(4):5174–5183, Aug 2018.
- [30] B. Abbott, R. Abbott, R. Adhikari, et al. Beating the Spin-Down Limit on Gravitational Wave Emission from the Crab Pulsar. *The Astrophysical Journal*, 683(1):L45, Aug 2008.
- [31] Margaret Millhouse, Lucy Strang, and Andrew Melatos. Search for gravitational waves from twelve young supernova remnants with a hidden Markov model in Advanced LIGO’s second observing run. *arXiv e-prints*, page arXiv:2003.08588, March 2020.
- [32] B. P. Abbott, R. Abbott, T. D. Abbott, et al. Search for Gravitational Waves from a Long-lived Remnant of the Binary Neutron Star Merger GW170817. *Astrophys. J.*, 875(2):160, April 2019.
- [33] L. Sun, A. Melatos, S. Suvorova, W. Moran, and R. J. Evans. Hidden Markov model tracking of continuous gravitational waves from young supernova remnants. *Phys. Rev. D*, 97(4):043013, February 2018.
- [34] A. Viterbi. Error bounds for convolutional codes and an asymptotically optimum decoding algorithm. *IEEE Transactions on Information Theory*, 13(2):260–269, April 1967.
- [35] Piotr Jaranowski, Andrzej Królak, and Bernard F. Schutz. Data analysis of gravitational-wave signals from spinning neutron stars: The signal and its detection. *Phys. Rev. D*, 58(6):063001, Sep 1998.
- [36] A. L. Watts, B. Krishnan, L. Bildsten, and B. F. Schutz. Detecting gravitational wave emission from the known accreting neutron stars. *Monthly Notices of the RAS*, 389:839–868, September 2008.
- [37] A. L. Watts and B. Krishnan. Detecting gravitational waves from accreting neutron stars. *Advances in Space Research*, 43:1049–1054, April 2009.
- [38] P. Ghosh, F. K. Lamb, and C. J. Pethick. Accretion by rotating magnetic neutron stars. I - Flow of matter inside the magnetosphere and its implications for spin-up and spin-down of the star. *Astrophys. J.*, 217:578–596, October 1977.
- [39] A. Melatos and A. Mastrano. Electromagnetic Spindown of a Transient Accreting Millisecond Pulsar During Quiescence. *Astrophys. J.*, 818:49, February 2016.
- [40] Lars Bildsten, Deepto Chakrabarty, John Chiu, et al. Observations of Accreting Pulsars. *The Astrophysical Journal Supplement Series*, 113(2):367–408, Dec 1997.

- [41] S. Bonazzola and E.ourgoulhon. Gravitational waves from pulsars: emission by the magnetic-field-induced distortion. *Astronomy and Astrophysics*, 312:675–690, Aug 1996.
- [42] A. Melatos and D. J. B. Payne. Gravitational Radiation from an Accreting Millisecond Pulsar with a Magnetically Confined Mountain. *The Astrophysical Journal*, 623(2):1044–1050, Apr 2005.
- [43] B. Haskell, L. Samuelsson, K. Glampedakis, and N. Andersson. Modelling magnetically deformed neutron stars. *Monthly Notices of the RAS*, 385:531–542, March 2008.
- [44] A. Mastrano and A. Melatos. Updated gravitational-wave upper limits on the internal magnetic field strength of recycled pulsars. *Monthly Notices of the RAS*, 421:760–767, March 2012.
- [45] Nathan K. Johnson-McDaniel and Benjamin J. Owen. Maximum elastic deformations of relativistic stars. *Physical Review D*, 88(4):044004, Aug 2013.
- [46] Benjamin J. Owen, Lee Lindblom, Curt Cutler, et al. Gravitational waves from hot young rapidly rotating neutron stars. *Phys. Rev. D*, 58(8):084020, Oct 1998.
- [47] Nils Andersson. A New Class of Unstable Modes of Rotating Relativistic Stars. *Astrophys. J.*, 502(2):708–713, Aug 1998.
- [48] A. Papitto, T. di Salvo, L. Burderi, et al. Timing of the accreting millisecond pulsar XTE J1814-338. *Monthly Notices of the RAS*, 375:971–976, March 2007.
- [49] P. Kaaret, E. H. Morgan, R. Vanderspek, and J. A. Tom-sick. Discovery of the Millisecond X-Ray Pulsar HETE J1900.1-2455. *Astrophys. J.*, 638:963–967, February 2006.
- [50] A. Sanna, F. Pintore, E. Bozzo, et al. Spectral and timing properties of IGR J00291+5934 during its 2015 outburst. *Monthly Notices of the RAS*, 466:2910–2917, Apr 2017.
- [51] M. A. Nowak, A. Paizis, J. Wilms, et al. IGR J00291+5934: an observation with Chandra. *The Astronomer’s Telegram*, 369(369):1, Dec 2004.
- [52] J. M. Hartman, A. Patruno, D. Chakrabarty, et al. The Long-Term Evolution of the Spin, Pulse Shape, and Orbit of the Accretion-powered Millisecond Pulsar SAX J1808.4-3658. *Astrophys. J.*, 675:1468–1486, March 2008.
- [53] A. Sanna, T. Di Salvo, L. Burderi, et al. On the timing properties of SAX J1808.4-3658 during its 2015 outburst. *Monthly Notices of the RAS*, 471:463–477, Oct 2017.
- [54] Duncan K. Galloway, Deepto Chakrabarty, Edward H. Morgan, and Ronald A. Remillard. Discovery of a High-Latitude Accreting Millisecond Pulsar in an Ultracompact Binary. *Astrophysical Journal, Letters*, 576(2):L137–L140, Sep 2002.
- [55] Roland Vanderspek, Ed Morgan, Geoff Crew, Carlo Graziani, and Motoko Suzuki. Possible new X-ray burst source detected by HETE. *The Astronomer’s Telegram*, 516:1, Jun 2005.
- [56] Motoko Suzuki, Nobuyuki Kawai, Toru Tamagawa, et al. Discovery of a New X-Ray Burst/Millisecond Accreting Pulsar, HETE J1900.1-2455. *Publications of the ASJ*, 59:263–268, Feb 2007.
- [57] Duncan K. Galloway, Michael P. Muno, Jacob M. Hartman, Dimitrios Psaltis, and Deepto Chakrabarty. Thermonuclear (Type I) X-Ray Bursts Observed by the Rossi X-Ray Timing Explorer. *Astrophysical Journal, Supplement*, 179(2):360–422, Dec 2008.
- [58] D. K. Galloway, E. H. Morgan, and D. Chakrabarty. Breaking the AMSP mould: the increasingly strange case of HETE J1900.1-2455. In R. Wijnands, D. Altamirano, P. Soleri, et al., editors, *American Institute of Physics Conference Series*, volume 1068 of *American Institute of Physics Conference Series*, pages 55–62, October 2008.
- [59] Richard N. Manchester and Joseph H. Taylor. *Pulsars*. 1977.
- [60] N. Degenaar, L. S. Ootes, M. T. Reynolds, R. Wijnands, and D. Page. A cold neutron star in the transient low-mass X-ray binary HETE J1900.1-2455 after 10 yr of active accretion. *Monthly Notices of the RAS*, 465:L10–L14, February 2017.
- [61] Duncan K. Galloway, Craig B. Markwardt, Edward H. Morgan, Deepto Chakrabarty, and Tod E. Strohmayer. Discovery of the Accretion-powered Millisecond X-Ray Pulsar IGR J00291+5934. *Astrophysical Journal, Letters*, 622(1):L45–L48, Mar 2005.
- [62] D. K. Galloway. Accretion-powered Millisecond Pulsar Outbursts. In F. D’Amico, J. Braga, and R. E. Rothschild, editors, *The Transient Milky Way: A Perspective for MIRAX*, volume 840 of *American Institute of Physics Conference Series*, pages 50–54, June 2006.
- [63] M. A. P. Torres, P. G. Jonker, D. Steeghs, et al. Observations of the 599 Hz Accreting X-Ray Pulsar IGR J00291+5934 during the 2004 Outburst and in Quiescence. *Astrophys. J.*, 672:1079–1090, January 2008.
- [64] Ron Remillard. ASM Observations of IGR J00291+5934. *The Astronomer’s Telegram*, 357:1, Dec 2004.
- [65] V. De Falco, L. Kuiper, E. Bozzo, et al. The 2015 outburst of the accretion-powered pulsar IGR J00291+5934: INTEGRAL and Swift observations. *Astronomy and Astrophysics*, 599:A88, Mar 2017.
- [66] Jacob M. Hartman, Duncan K. Galloway, and Deepto Chakrabarty. A Double Outburst from IGR J00291+5934: Implications for Accretion Disk Instability Theory. *Astrophys. J.*, 726(1):26, Jan 2011.
- [67] A. Papitto, A. Riggio, L. Burderi, et al. Spin down during quiescence of the fastest known accretion-powered pulsar. *Astronomy and Astrophysics*, 528:A55, Apr 2011.
- [68] G. Boella, R. C. Butler, G. C. Perola, et al. BeppoSAX, the wide band mission for X-ray astronomy. *Astronomy and Astrophysics, Supplement*, 122:299–307, Apr 1997.
- [69] D. K. Galloway and A. Cumming. Helium-rich Thermonuclear Bursts and the Distance to the Accretion-powered Millisecond Pulsar SAX J1808.4-3658. *Astrophys. J.*, 652:559–568, November 2006.
- [70] Peter Bult, Deepto Chakrabarty, Zaven Arzoumanian, et al. Timing the pulsations of the accreting millisecond pulsar SAX J1808.4-3658 during its 2019 outburst. *arXiv e-prints*, page arXiv:1910.03062, October 2019.
- [71] A. Marino, T. Di Salvo, A. F. Gambino, et al. Evidence of a non-conservative mass transfer for XTE J0929-314. *Astronomy and Astrophysics*, 603:A137, Jul 2017.
- [72] C. B. Markwardt and J. H. Swank. XTE J1814-338. *IAU Circulars*, 8144, June 2003.
- [73] M. I. Krauss, Z. Wang, A. Dullighan, et al. The X-Ray Position and Optical Counterpart of the Accretion-powered Millisecond Pulsar XTE J1814-338. *Astrophys. J.*, 627:910–914, July 2005.
- [74] T. E. Strohmayer, C. B. Markwardt, J. H. Swank, and J. in’t Zand. X-Ray Bursts from the Accreting Millisecond Pulsar XTE J1814-338. *Astrophysical Journal, Letters*, 596:L67–L70, October 2003.
- [75] Umin Lee. Non-axisymmetric low-frequency oscillations of rotating and magnetized neutron stars. *Monthly Notices of the RAS*, 405(3):1444–1457, Jul 2010.

- [76] A. Melatos, J. A. Douglass, and T. P. Simula. Persistent Gravitational Radiation from Glitching Pulsars. *Astrophys. J.*, 807(2):132, July 2015.
- [77] D. I. Jones. Gravitational wave emission from rotating superfluid neutron stars. *Monthly Notices of the RAS*, 402(4):2503–2519, Mar 2010.
- [78] Joseph Betzwieser and LIGO Scientific Collaboration. Expanding the Gravitational Wave Search for the Crab Pulsar. In *American Astronomical Society Meeting Abstracts #213*, volume 213 of *American Astronomical Society Meeting Abstracts*, page 477.06, Jan 2009.
- [79] B. P. Abbott, R. Abbott, T. D. Abbott, et al. Narrow-band search for gravitational waves from known pulsars using the second LIGO observing run. *Physical Review D*, 99(12):122002, Jun 2019.
- [80] B. P. Abbott, R. Abbott, T. D. Abbott, et al. First low-frequency Einstein@Home all-sky search for continuous gravitational waves in Advanced LIGO data. *Physical Review D*, 96(12):122004, Dec 2017.
- [81] J. Ming, M. A. Papa, A. Singh, et al. Results from an Einstein@Home search for continuous gravitational waves from Cassiopeia A, Vela Jr., and G347.3. *Physical Review D*, 100(2):024063, Jul 2019.
- [82] Santiago Caride, Ra Inta, Benjamin J. Owen, and Binod Rajbhandari. How to search for gravitational waves from r-modes of known pulsars. *Phys. Rev. D*, 100(6):064013, Sep 2019.
- [83] Liudmila Fesik and Maria Alessandra Papa. First Search for r-mode Gravitational Waves from PSR J0537-6910. *Astrophys. J.*, 895(1):11, May 2020.
- [84] R. Prix. LIGO Report T0900149: The F-statistic and its implementation in ComputeFStatistic_v2, Jun 2011.
- [85] P. Leaci and R. Prix. Directed searches for continuous gravitational waves from binary systems: Parameter-space metrics and optimal Scorpius X-1 sensitivity. *Phys. Rev. D*, 91(10):102003, May 2015.
- [86] Liam Dunn, Patrick Clearwater, Andrew Melatos, and Karl Wette. Graphics processing unit implementation of the F-statistic for continuous gravitational wave searches. 2020. In prep.
- [87] Bennett K. Link and Richard I. Epstein. Mechanics and Energetics of Vortex Unpinning in Neutron Stars. *The Astrophysical Journal*, 373:592, Jun 1991.
- [88] A. Melatos. Fast Fossil Rotation of Neutron Star Cores. *The Astrophysical Journal*, 761(1):32, Dec 2012.
- [89] J. Papaloizou and J. E. Pringle. Gravitational radiation and the stability of rotating stars. *Monthly Notices of the RAS*, 184:501–508, Aug 1978.
- [90] R. V. Wagoner. Gravitational radiation from accreting neutron stars. *Astrophysical Journal*, 278:345–348, Mar 1984.
- [91] LIGO Scientific Collaboration. LIGO Algorithm Library - LALSuite. free software (GPL), 2018.
- [92] P. B. Covas, A. Effler, E. Goetz, et al. Identification and mitigation of narrow spectral artifacts that degrade searches for persistent gravitational waves in the first two observing runs of Advanced LIGO. *Phys. Rev. D*, 97(8):082002, April 2018.
- [93] Michele Vallisneri, Jonah Kanner, Roy Williams, Alan Weinstein, and Branson Stephens. The LIGO Open Science Center. In *Journal of Physics Conference Series*, volume 610 of *Journal of Physics Conference Series*, page 012021, May 2015.
- [94] Swinburne University of Technology. OzSTAR Supercomputing. <https://supercomputing.swin.edu.au/ozstar/>. Accessed: 2020-04-03.
- [95] Intel. Intel Xeon Gold 6140 Processor. <https://ark.intel.com/content/www/us/en/ark/products/120485/intel-xeon-gold-6140-processor-24-75m-cache-2-30-ghz.html>.
- [96] NVIDIA. NVIDIA TESLA P100 GPU Accelerator. <https://images.nvidia.com/content/tesla/pdf/nvidia-tesla-p100-PCIe-datasheet.pdf>. Accessed: 2020-04-03.
- [97] J. M. Hartman, A. Patruno, D. Chakrabarty, et al. A Decade of Timing an Accretion-powered Millisecond Pulsar: The Continuing Spin Down and Orbital Evolution of SAX J1808.4-3658. *Astrophys. J.*, 702:1673–1678, September 2009.
- [98] A. Patruno, P. Bult, A. Gopakumar, et al. Accelerated Orbital Expansion and Secular Spin-down of the Accreting Millisecond Pulsar SAX J1808.4-3658. *Astrophysical Journal, Letters*, 746:L27, February 2012.
- [99] Q. Z. Liu, J. van Paradijs, and E. P. J. van den Heuvel. A catalogue of low-mass X-ray binaries in the Galaxy, LMC, and SMC (Fourth edition). *Astronomy and Astrophysics*, 469(2):807–810, Jul 2007.

Appendix A: SFT Lengths

The SFTs used in this search are of duration $T_{\text{SFT}} = 1800\text{s}$, identical to those used in searches for Scorpius X-1 [24]. The targets considered in this search have typically much shorter P than Scorpius X-1 ($P = 68\,023.86048 \pm 0.0432\text{s}$ [29]). A shorter P requires commensurately shorter SFTs, if the \mathcal{F} -statistic is used for the HMM emission probability. This is not the case for the \mathcal{J} -statistic used in this paper, because it weights and sums the Doppler-shifted orbital sidebands based on the orbital parameters of the target in a manner that is coherent with respect to orbital phase. In this appendix we run a short test to verify that the \mathcal{J} -statistic is calculated accurately with 1800 s SFTs.

Following Eq. (C2) in Ref. [85], the maximum length of an SFT for computing the \mathcal{F} -statistic is

$$T_{\text{SFT}}^2(f) \leq \frac{6\sqrt{5}\mu_{\text{SFT}}}{\pi a_0 f \Omega^2}, \quad (\text{A1})$$

where μ_{SFT} is the SFT mismatch (which we choose to be 0.01). The LMXB target with the shortest P considered here is XTE J0929-314 [$P = 2614.746(3)\text{s}$]. For XTE J0929-314, Eq. A1 gives $T_{\text{SFT}} \leq 177\text{s}$ for the highest frequency searched for this target.

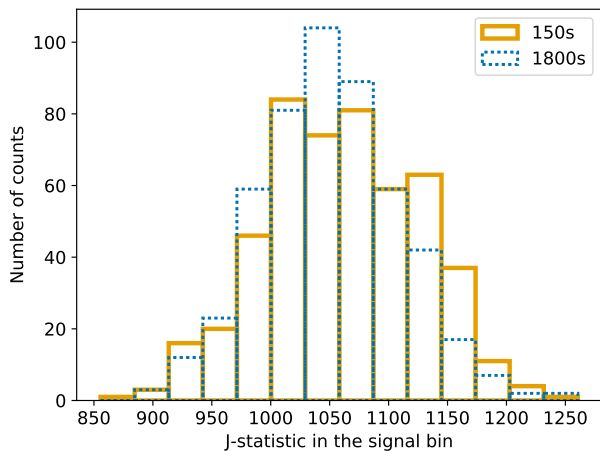


FIG. 3: \mathcal{J} -statistic versus SFT length for a signal injected with the orbital parameters of XTE J0929-314, $f_{\star} = 370.210508594\text{Hz}$, and $h_0 = 1 \times 10^{-24}$. The histogram bins refer to the value of the \mathcal{J} -statistic in the frequency bin of the injection for 500 noise realisations. The orange-solid and blue-dotted bars correspond to $T_{\text{SFT}} = 150\text{s}$ and 1800s respectively.

Using `lalapps.Makefakedata_v4` we generate simulated SFTs containing Gaussian noise and an injected signal with the same orbital parameters as XTE J0929-314 (see Table I). The signal is injected with a frequency of $2f_{\star} = 370.210508594\text{Hz}$ and a gravitational wave strain of $h_0 = 1 \times 10^{-24}$. For the purposes of this test we

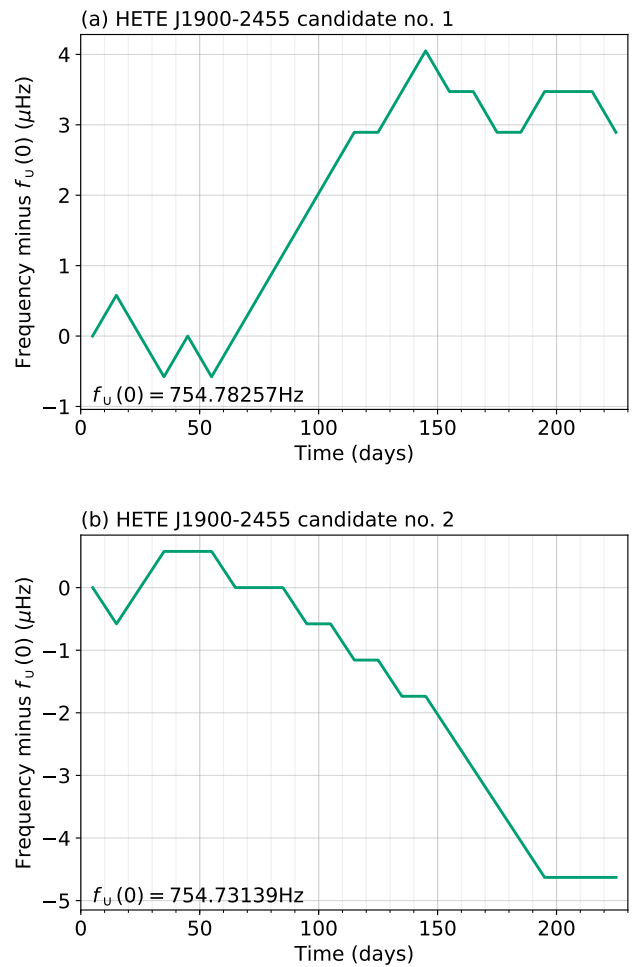


FIG. 4: Frequency path for the two HETE J1900.1-2455 candidates. The horizontal axis shows the time in days since the beginning of O2. The vertical axis shows the frequency of the path f_{U} with the starting frequency of the path subtracted ($f_{\text{U}}(0)$, displayed in the bottom-left corner in the figure).

use a 10 d dataset with $T_{\text{obs}} = T_{\text{drift}}$ and hence $N_T = 1$. Using identical injection parameters, SFTs are generated with $T_{\text{SFT}} = 1800\text{s}$ and 150s using 500 Gaussian noise realisations. We choose 150s for the shorter SFTs to give a whole number of SFTs for a 10 day dataset. The \mathcal{J} -statistic in the frequency bin containing the signal is computed and the \mathcal{J} -statistic distributions from the two SFT lengths are compared.

The result is shown in Fig. 3. The \mathcal{J} -statistic distributions for the 1800s and 150s SFTs are shown by the blue-dot and orange-solid bars respectively. We see that the distributions are similar, with a Kullback-Leibler divergence of 0.0015 using the binning in the figure. That is, the \mathcal{J} -statistic does not depend on T_{SFT} in the regime relevant to this paper.

TABLE VI: Candidates returned by the search for each of the five LMXBs. The table shows the orbital period (P), projected semi-major axis (a_0), and time of ascension (T_{asc}) for the search template. The Viterbi score (S_{\cup}) and terminating frequency [$f_{\cup}(t = N_T)$] of the template Viterbi path are shown in the fifth and sixth column respectively. The seventh and eighth columns indicate whether the template’s Viterbi score exceeds the Gaussian (S_{th}^{G}) and off-target $S_{\text{th}}^{\text{OT}}$ thresholds respectively (\checkmark for yes, \times for no). The right-most four columns summarize the veto outcomes (\checkmark for survives and \times for vetoed). The two templates marked with * are nearly above-threshold templates which are included in the veto analysis for safety against rounding errors because they have $S_{\cup} \approx S_{\text{th}}^{\text{OT}}$. The veto outcomes for nearly above-threshold templates are indicated in parentheses. Without including the nearly above-threshold templates, there are five survivors.

Candidate number	P (s)	a_0 (lt-s)	T_{asc} (GPS time)	S_{\cup}	$f_{\cup}(t = N_T)$ (Hz)	Above threshold?		Survives veto?			
						S_{th}^{G}	$S_{\text{th}}^{\text{OT}}$	#1	#2	#3	#4
HETE J1900.1-2455											
1	4995.258	0.01841	1164560065.80899	8.54656	754.78257333	\checkmark	\checkmark	\checkmark	\checkmark	\checkmark	\checkmark
2	4995.273	0.01841	1164559919.78652	8.78604	754.73138932	\checkmark	\checkmark	\checkmark	\checkmark	\checkmark	\checkmark
IGR J00291+5934											
1	8844.05	0.0649905	1164557590.28572	8.30371	299.54681334	\checkmark	\times	\times	-	-	-
2	8844.095	0.0649905	1164557538.85715	8.55464	299.54681276	\checkmark	\times	\times	-	-	-
3	8844.14	0.0649905	1164557127.42857	8.30045	299.55189494	\checkmark	\times	\times	-	-	-
4*	8844.125	0.0649905	1164557585.14285	8.46619	598.95731631	\times	\times	(\checkmark)	(\checkmark)	(\checkmark)	(\checkmark)
5	8844.112	0.0649905	1164557556.85714	9.03732	1197.76730242	\times	\checkmark	\checkmark	\checkmark	\checkmark	\checkmark
SAX J1808.4-3658											
1	7249.155	0.06281	1164560394.28571	7.49118	200.35371679	\times	\checkmark	\times	-	-	-
2*	7249.155	0.06281	1164560531.00000	7.58480	400.60481930	\times	\times	(\checkmark)	(\checkmark)	(\checkmark)	(\checkmark)
3	7249.137	0.06281	1164560405.33333	7.90013	534.45904849	\checkmark	\checkmark	\checkmark	\checkmark	\checkmark	\checkmark
XTE J1814-338											
1	15388.7229	0.390633	1164547409.69231	7.03362	314.46162299	\times	\checkmark	\checkmark	\checkmark	\times	-
2	15388.7229	0.390633	1164547397.23077	7.35219	628.69675855	\checkmark	\checkmark	\checkmark	\checkmark	\checkmark	\checkmark

Appendix B: Complete search results

This appendix summarises the search results and veto outcomes for the five LMXB targets. Table VI lists the ten candidates described in Sec. VII. Columns two, three, and four show the orbital parameters (P , a_0 , and T_{asc}) of each candidate template. The fifth and sixth columns show the Viterbi score and terminating frequency path respectively for the candidate template. The seventh and eighth columns indicate whether the candidate exceeds S_{th}^{G} and $S_{\text{th}}^{\text{OT}}$ respectively. The final four columns indicate whether the candidate survives vetoes 1–4. The two additional templates marked with * indicate the nearly above-threshold templates with $S_{\cup} \approx S_{\text{th}}^{\text{OT}}$ which we include in the veto procedure to avoid being misled by rounding errors (see also Sec. VII).

The search results for HETE J1900.1-2455 are shown in Fig. 2 of the main paper. Figure 4 shows the frequency path for the twp HETE J1900.1-2455 candidates. The

horizontal axis shows the time in days and the vertical axis shows the frequency of the path f_{\cup} with $f_{\cup}(t = 0)$ subtracted.

Figure 5 shows the search results for IGR J00291+5934 identically laid out to the HETE J1900.1-2455 results shown in Fig. 2. In brief, the four panels of each figure show the $\{1/2, 1, 4/3, 2\}f_*$ sub-bands, each marker indicates the terminating frequency of the best Viterbi path for each orbital template with the associated Viterbi score, the vertical lines show the 0.30 FAP per-template thresholds, and the horizontal lines and shading indicate the presence of instrumental noise lines. Frequency paths for the five IGR J00291+5934 templates listed in Table VI are shown in Fig. 6. Search results and paths (for targets with candidates) are also shown for SAX J1808.4-3658 (Figs. 7 and 8), XTE J0929-314 (Fig. 9), and XTE J1814-338 (Figs. 10 and 11).

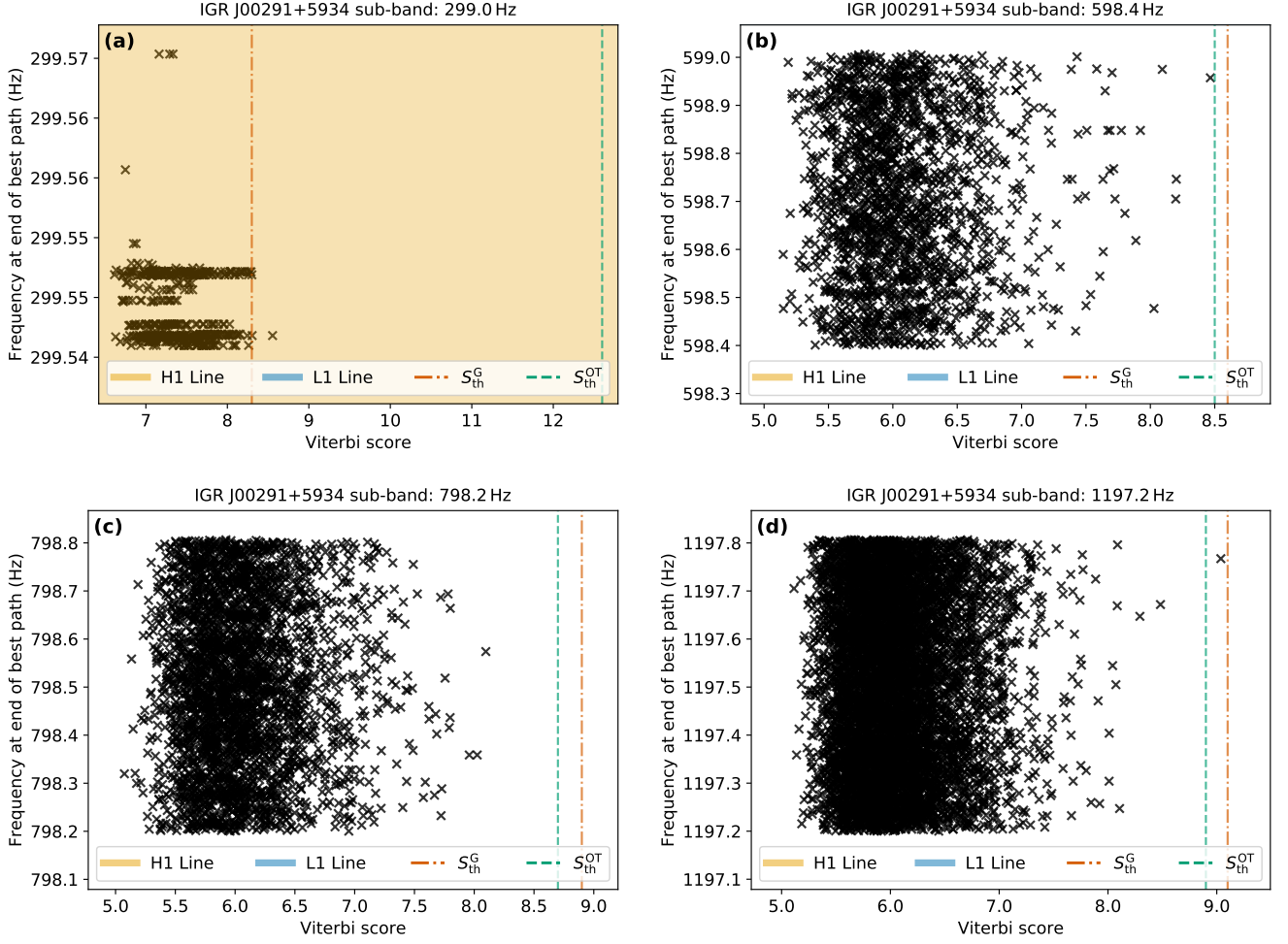


FIG. 5: Search results for IGR J00291+5934, laid out as in Fig. 2. The reader is reminded that the shaded band in the panel (a) indicates the presence of an instrumental noise line and the sub-bands $f_*/2$, f_* , $4f_*/3$, and $2f_*$ are shown in panels (a), (b), (c), and (d) respectively. The instrumental noise line is due to a violin mode in the Hanford observatory which peaks at 299.60 Hz and has range 299.35–299.85 Hz (covering the entire plotted region). The veto procedure is applied to five templates (three in the $f_*/2$ sub-band, one in the $2f_*$ sub-band, and the highest scoring in the f_* sub-band).

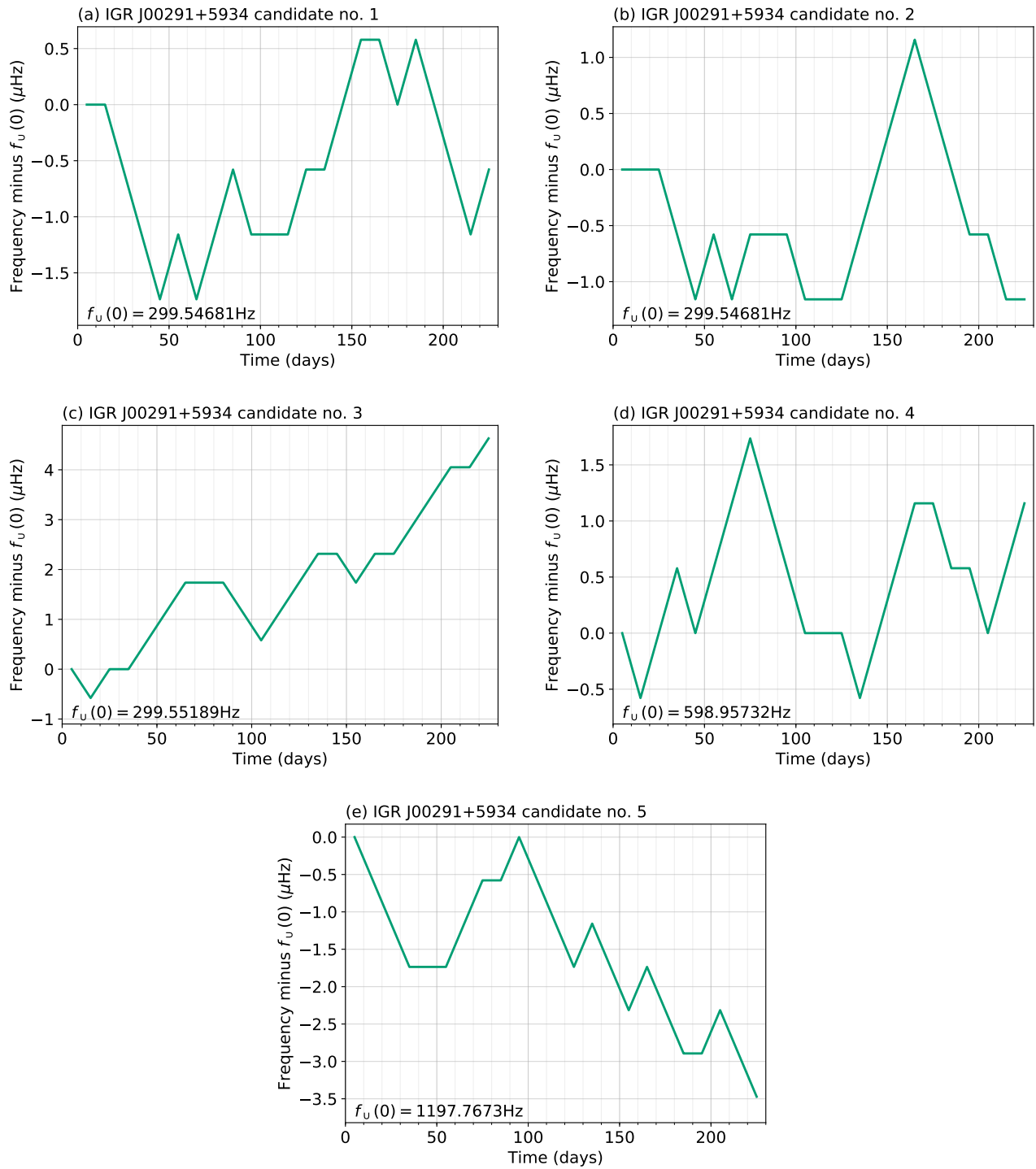


FIG. 6: IGR J00291+5934 candidate frequency paths laid out identically to Fig. 4.

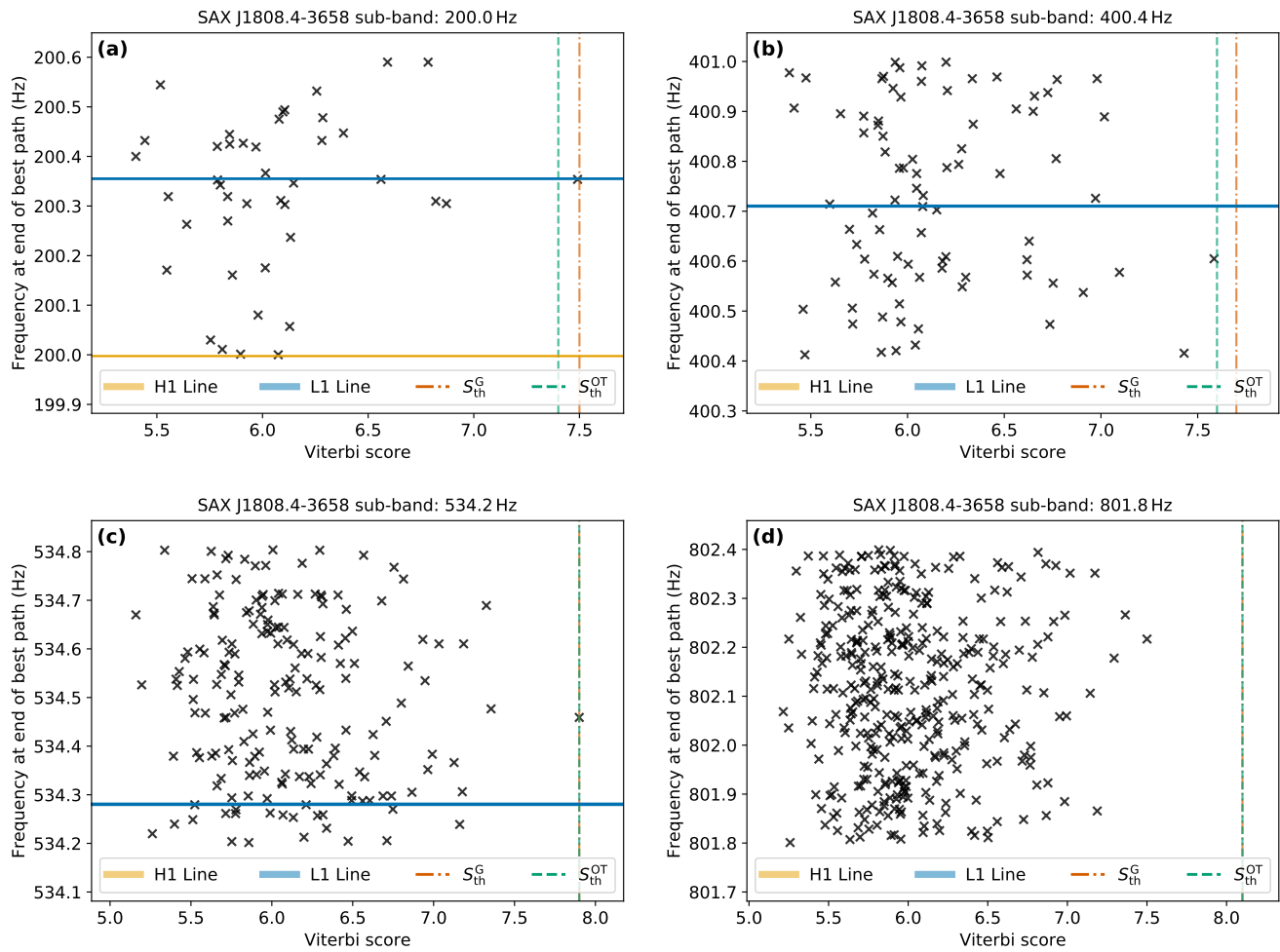


FIG. 7: Search results for SAX J1808.4-3658, laid out as in Fig. 2.

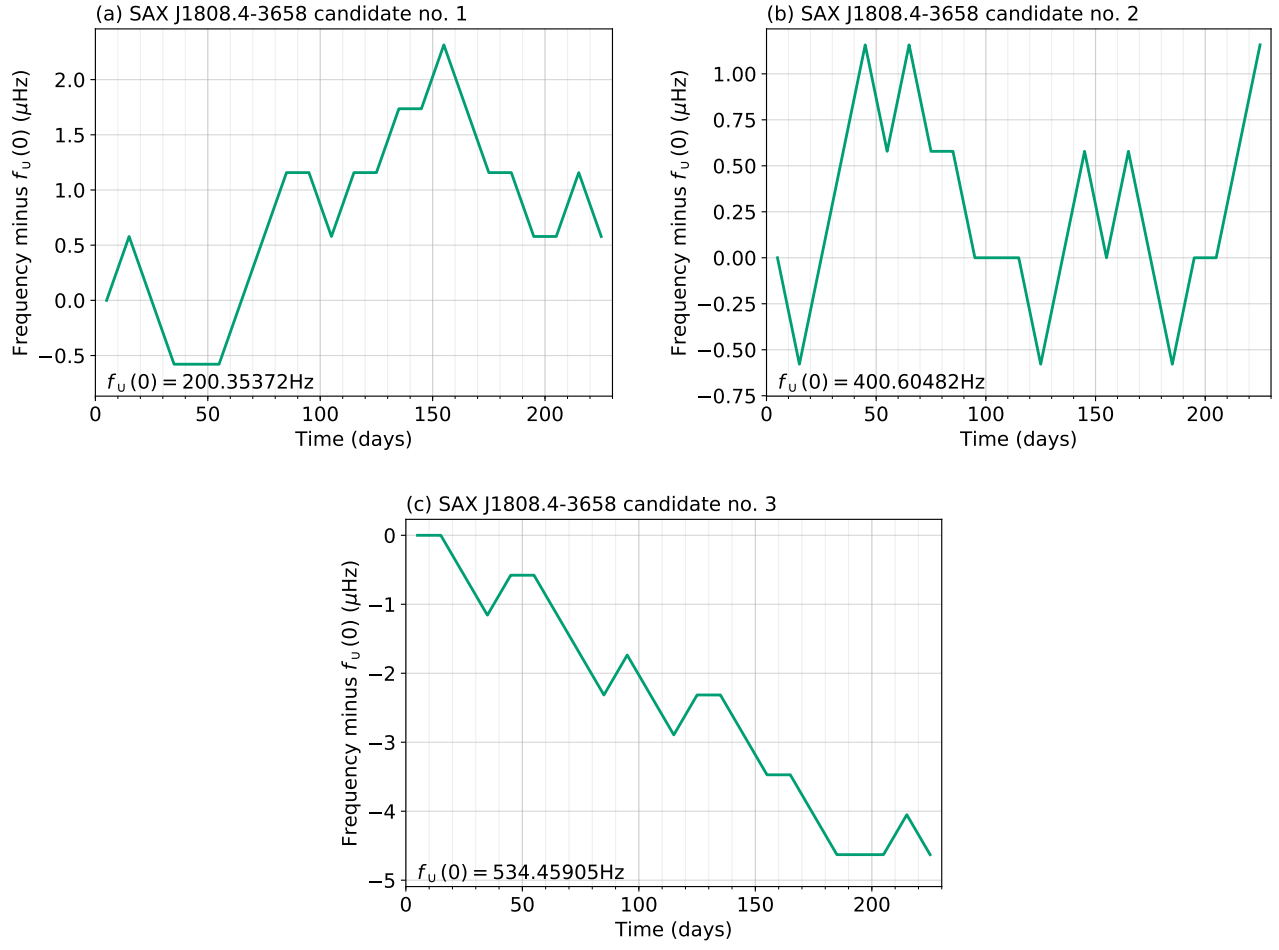


FIG. 8: SAX J1808.4-3658 candidate frequency paths laid out identically to Fig. 4.

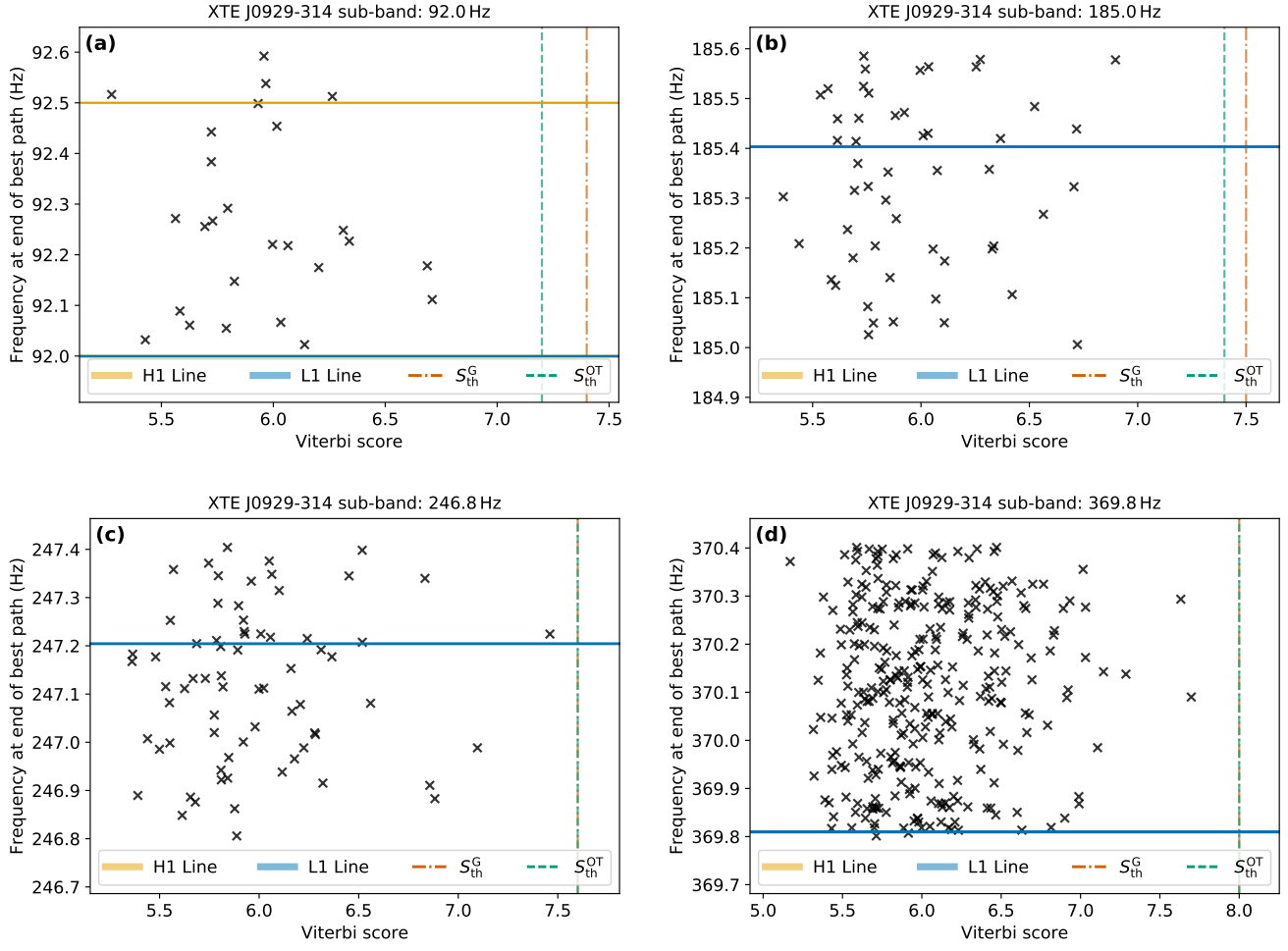


FIG. 9: Search results for XTE J0929-314, laid out as in Fig. 2.

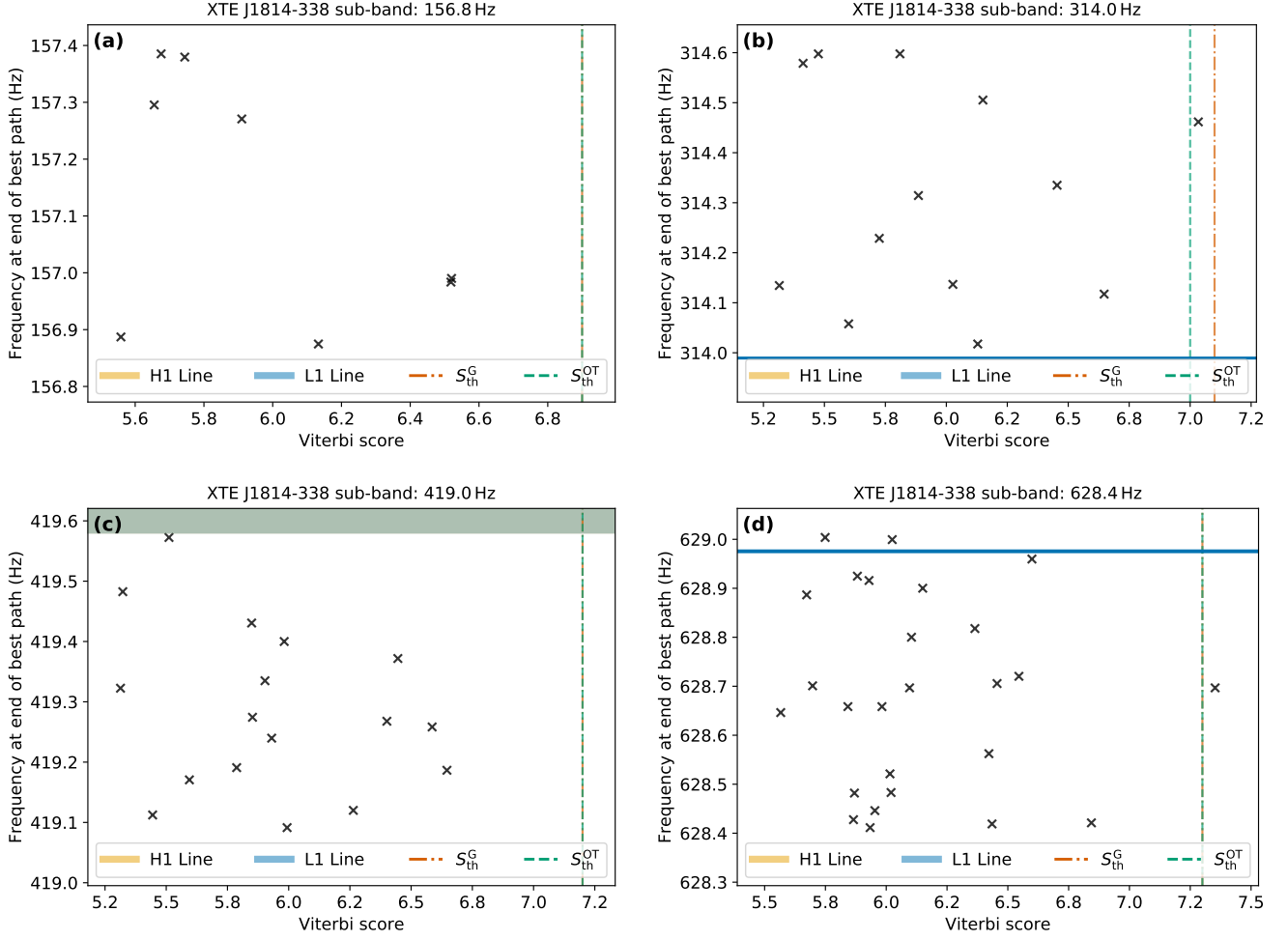


FIG. 10: Search results for XTE J1814-338, laid out as in Fig. 2. The mixed-color shading at high frequencies in panel (c) is the overlap of instrumental lines from Hanford and Livingston.

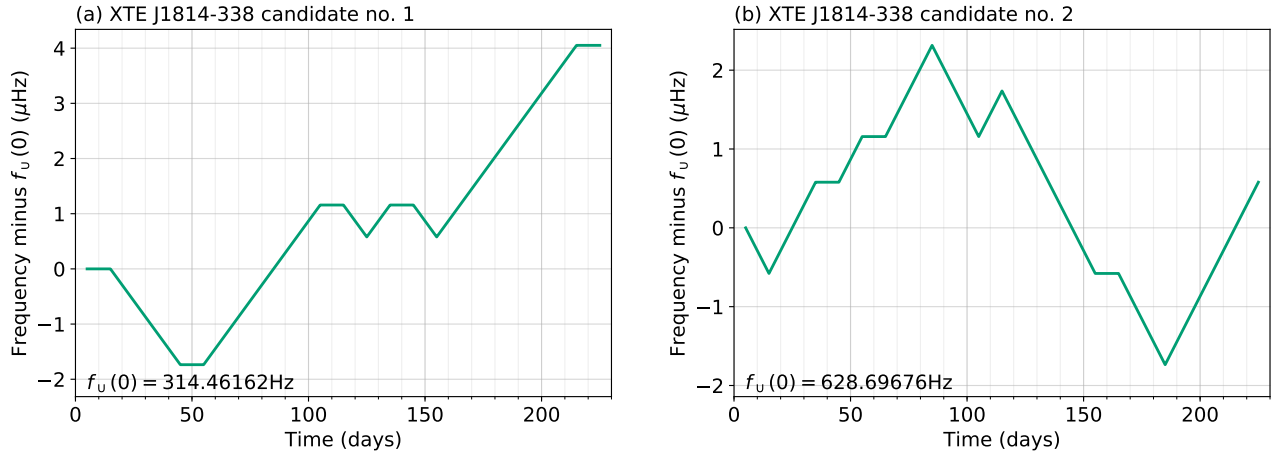


FIG. 11: XTE J1814-338 candidate frequency paths laid out identically to Fig. 4.